Experimental Study of Turbulent Flow Around Trapezoidal Cylinders in Uniform Flow

By

Jinhao Kang

A Thesis submitted to the Faculty of Graduate Studies of

The University of Manitoba

in Partial Fulfilment of the Requirements of the Degree of

MASTER OF SCIENCE

Department of Mechanical Engineering

University of Manitoba

Winnipeg, Manitoba

Canada

ABSTRACT

This thesis presents an experimental investigation on the effects of streamwise aspect ratio (AR) on asymmetric wake flows around right-angled trapezoidal cylinders with AR (upper cylinder length to height ratio) = 1, 2, 3, 4, and 5 using a particle image velocimetry (PIV) technique. The Reynolds number based on the free-stream velocity and cylinder height was 14700. The flow characteristics are examined in terms of the mean flow, Reynolds stresses, turbulent kinetic energy (TKE), turbulent transport and production term of TKE, probability density function (PDF), joint probability density function (JPDF) and two-point autocorrelations.

The results show that the primary vortex in the AR1 and AR2 cases extends into the wake region but is confined to the surface of AR ≥ 3 and two asymmetric wake vortexes are only observed in these longer cases. Dual peaks of elevated streamwise Reynolds normal stress are observed in the wake region, irrespective of the aspect ratio. The magnitudes of the Reynolds stresses, TKE, and production term of TKE in the wake region are higher in the AR1, AR2 and AR3 cases compared to the AR4 and AR5 cases. The turbulent transport of TKE by streamwise and vertical fluctuating velocities show switches sign along the mean separating streamline, regardless of aspect ratios. The PDF distributions show a bimodal asymmetric shape in the shorter cases but a nearly Gaussian distribution in the AR5 case. Two-point autocorrelations of the streamwise and vertical velocity fluctuations show that the spatial coherency of the turbulent structures is highly sensitive to the streamwise aspect ratio and reference locations. Systematic comparisons between the present asymmetric results and symmetric wakes generated by rectangular cylinders with similar aspect ratios and Reynolds number show significant differences between the asymmetric and symmetric wakes, especially for the shorter cases.

ACKNOWLEDGMENTS

I am deeply grateful to my academic advisor, Professor Mark F. Tachie, for his invaluable support, encouragement, and guidance for the past three years.

I would also like to express my gratitude to all my colleagues at the Turbulence and Hydraulic Engineering Laboratory for their help, friendship, and motivation. I am thankful to Sedem Kumahor for his valuable support and assistance in both my undergraduate and graduate research. I am also thankful to Dr. Xingjun Fang for his valuable help and encouragement throughout my master's program.

Lastly, I am deeply indebted to my parents, Junfang Shi and Zhide Kang, as well as my uncle, Changhua Shi, for their unwavering patience, love, and encouragement.

TABLE OF CONTENTS

LIST OF TABLES

LIST OF FIGURES

NOMENCLATURE

d_p	Diameter of the seeding particles
Fr	Froude number
g	Acceleration due to gravity
h	Vertical height of the cylinder
H_u	Water Depth
L	Streamwise length of the rectangular cylinder and the upper streamwise length of the trapezoidal cylinder
L_1	Fixed bottom length of the trapezoidal cylinder
L_r	Recirculation length
L_T	Reattachment length
$L_{u'}$	Wake formation length based on the maximum location of streamwise Reynolds normal stress
L_u^x	Integral length scale based on two-point autocorrelation of streamwise fluctuating velocity
$L_{v'}$	Wake formation length based on the maximum location of vertical Reynolds normal stress
L_v^x	Integral length scale based on two-point autocorrelation of vertical fluctuating velocity
N	Number of samples

P_T	Production term of turbulent kinetic energy
Re	Reynolds number based on cylinder height and free-stream velocity
R_{uu}	Two-point autocorrelation of streamwise fluctuating velocity
R_{vv}	Two-point autocorrelation of vertical fluctuating velocity
S_k	Stokes number
Tu	Turbulence intensity
U	Streamwise mean velocity
U_{CL}	Streamwise mean velocity along the horizontal centerline of the cylinder
U_b	Maximum backflow velocity
U_e	Free-stream velocity
U_{max}	Maximum streamwise mean velocity
U_s	Slip velocity
V	Vertical mean velocity
w	Spanwise width of the cylinder
x	Streamwise coordinate
Y	Vertical distance from the vortex core in the near wake region to the horizontal centerline of the cylinder
y	Vertical coordinate
Z_c	Confidence coefficient

Greek Letters

α	Constant angle of the trapezoidal cylinder
δ_p	Boundary layer thickness formed on the plate at free surface
ξ_U	Relative uncertainty in the streamwise mean velocity
$\xi_{u_i u_i}$	Relative uncertainty in the Reynolds normal stresses
ξ_{uv}	Relative uncertainty in the Reynolds shear stress
ρ_f	Density of water
ρ_p	Density of seeding particles
τ_f	Characteristic time scale
τ_p	Relaxation time
ν	Kinematic viscosity of water
ω_Z	Mean spanwise vorticity

Abbreviations

AR	Streamwise aspect ratio
BR	Blockage ratio
CMOS	Complementary metal oxide semiconductor
DNS	Direct numerical simulation

FOV	Field of view
HWA	Hot wire anemometry
IA	Interrogation area
JPDF	Joint probability density function
LDV	Laser Doppler velocimetry
LES	Large eddy simulation
PDF	Probability density function
PIV	Particle image velocimetry
POD	Proper orthogonal decomposition
TKE	Turbulent kinetic energy

Subscripts and Superscripts

$(\cdot)'$	Fluctuating velocity component
$\overline{(\cdot)}$	Time-averaged component
$(\cdot)_{rms}$	Root-mean-square value

1. INTRODUCTION

In this chapter, the motivation and background of the present study as well as the outline of the reminder of this thesis, are presented.

1.1 Motivation and Background

Flow separation and reattachment induced by bluff bodies have received significant research attention in the fluid dynamics community due to their complex nature and wide-spread occurrence in many industrial and environmental applications. As shown in Figure 1.1, typical examples of such flows include wind flow around elevated walkways, separated airflow induced by ground vehicles, water current over pipelines laid on the seabed and unsteady wind flow induced by wind turbines. A thorough understanding of the flow characteristics and coherent structures formed around these bluff bodies is a prelude to the efficient design of the above mentioned and many other fluid engineering applications.

When a square cylinder is placed in a uniform flow, for example, the oncoming flow separates and accelerates past the upper and lower leading edges of the cylinder due to the surface discontinuities which force separation, regardless of the local pressure gradient (Moore et al., 2019a). According to Okajima (1982), Kiya and Sasaki (1983), and Bearman and Morel (1983), when the Reynolds number ($\mathrm{Re} = U_e h/\nu$, where U_e and ν are free-stream velocity and kinematic viscosity, respectively) is beyond 150, the separation point is fixed at both the upper and lower leading edges of the cylinder. The separated shear layers from the upper and lower leading edges are shed directly into the wake region. Schmid and Henningson (2001) reported that the small-scale Kelvin-Helmholtz (KH) vortical structures formed near the leading edge grow in an

(a)

(b)

(c)

(d)

Figure 1.1: Pictures of the elevated walkway (Heathcote, 2017), (a), vehicle in the airflow (Pachpute, 2022), (b), pipelines on the seabed (University of Aberdeen, 2023), (c), and the wind turbine (Oboe, 2023), (d).

unbounded manner and subsequently pair up within the shear layers. Consequently, the upper and lower separated shear layers undergo transition from laminar to turbulence and move across the centerline of the cylinder in the wake region, shedding alternatively from each side of the cylinder. These alternating large-scale vortical structures are the well-known von-Kármán (VK) vortex street in the cylinder wake region (Moore et al., 2019a; Addai et al., 2022). A depiction of the von Kármán vortex street in the wake of a square cylinder from the DNS simulation by Wu et al. (2016) at a Reynolds number of Re = 2000 is shown in Figure 1.2.

According to Okajima (1982), Durao et al. (1988), Lyn et al. (1995), Aleyasin et al. (2021), Kumahor and Tachie (2022) and Liu et al. (2022a), the flow dynamics of the wake flow induced by bluff bodies can be significantly influenced by many factors, including the geometry of the

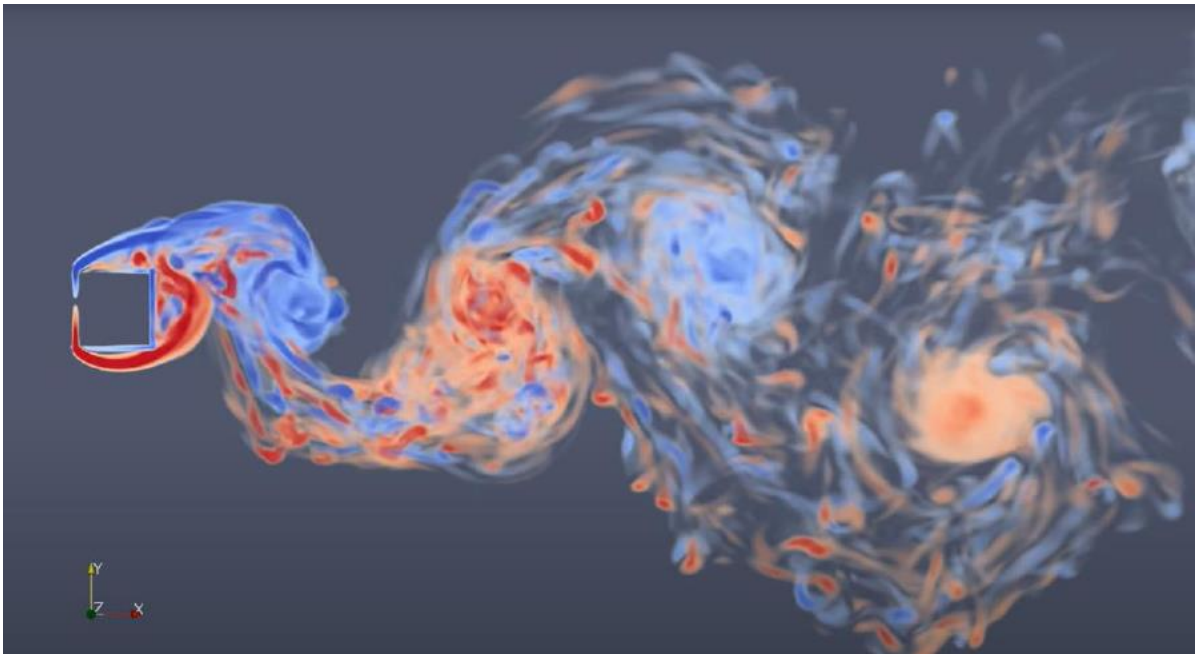

Figure 1.2: Depiction of the von Kármán vortex street in the wake region of a square cylinder (Wu et al., 2016).

bluff body, Reynolds number and the oncoming turbulence intensity. Figure 1.3 shows the schematics of the mean flow features over and behind a square cylinder (a), and a right-angled trapezoidal cylinder (b), immersed in a uniform flow with a free-stream velocity, U_e. The streamwise aspect ratio (AR) of both square and trapezoidal cylinders are defined as, AR = L/h, where h is the cylinder height and L is the streamwise length of the square cylinder and the upper length of the trapezoidal cylinder, respectively. Since the flow topology is symmetric about the horizontal centerline of the square cylinder (Moore et al., 2019a; Kumahor and Tachie, 2022; Chalmers et al., 2022; Liu et al., 2022a), only the upper half is shown in Figure 1.3. The oncoming flow separates at the leading edge and forms a separation bubble over the square cylinder, which is hereafter referred to as the primary vortex (PV). Flow separation also occurs at the leading edge of the trapezoidal cylinder (with AR = 1), but the primary vortex in the trapezoidal case starts at

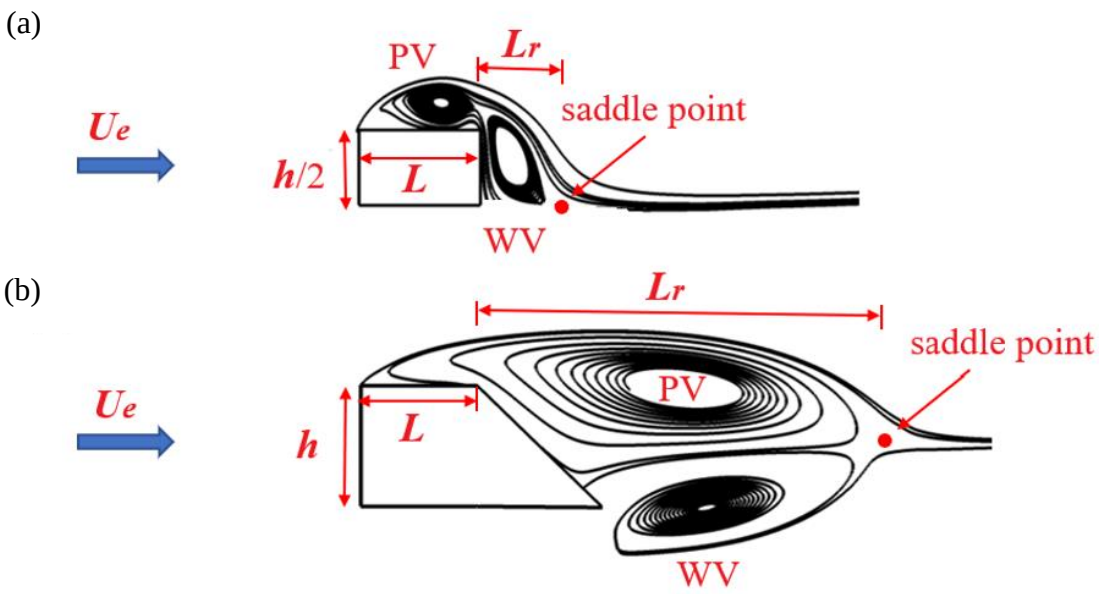

Figure 1.3: Schematics of the mean flow features over and behind a square cylinder and a right-angled trapezoidal cylinder with AR= 1.

the leading edge, extends along the top surface and into the wake region. In the near wake region, two symmetric recirculating bubbles are formed behind the square cylinder and are hereafter referred to as the wake vortex (WV). However, the wake vortices are asymmetric about the horizontal centerline behind the trapezoidal cylinder due to the modified trailing surface. The mean recirculation length, L_r, used to determine the size of the wake vortex, is defined as the streamwise length measured from the upper trailing edge of the cylinder to the end of the recirculation region indicated by a saddle point.

Over the past decades, symmetric wake flows generated by circular cylinders as well as square, and rectangular cylinders in uniform flow have received significant research attention (Dargahi, 1989; Yao et al., 2019; Kumahor and Tachie, 2022; Liu et al., 2022b). In contrast, the present understanding of asymmetric turbulent flows induced by asymmetric bluff bodies is comparatively deficient. In the current study, the right-angled trapezoidal cylinders of varying

streamwise extents are used as a canonical body geometry to investigate the characteristics of the asymmetric bluff body wake. To this end, a planar particle image velocimetry (PIV) technique is employed to perform whole-field velocity measurements to examine the spatial characteristics of the separated shear layer and the wake flow behind the cylinders.

1.2 Thesis Outline

The remainder of this thesis is organized as follows: the literature review is presented in Chapter 2 while the experimental setup and measurement procedure are described in Chapter 3. The results and discussion are presented in Chapter 4, and the major findings and conclusions as well as the recommendations for future work are summarized in Chapter 5.

2. LITERATURE REVIEW

A review of the pertinent literature on symmetric and asymmetric wake flows induced by bluff bodies as well as the objectives of the present study are presented in this chapter.

Extensive investigations on the flow around cylinders in a uniform flow have been conducted in the past. Due to their geometric simplicity, flow around circular cylinders (Kiya and Tamura, 1989; Williamson, 1996; Khabbouchi et al., 2014) and rectangular cylinders (Okajima, 1982; Kiya and Sasaki, 1983; Bearman and Morel, 1983; Durao et al., 1988; Frank et al., 1990; Lyn et al., 1995) has been extensively studied. Although the wake flows induced by these cylinders are all symmetric about the horizontal centerline of the cylinder (Anagnostopoulos et al., 1996; Dong et al., 2006; Moore et al., 2019a; Kumahor and Tachie, 2023b), significant differences are observed among these flows. The separation point, for example, moves upstream of the circular cylinder with increasing Reynolds number (Achenbach, 1968), but is fixed at the sharp leading edge of rectangular cylinders, when the Reynolds number is beyond 150 (Bearman and Moreal, 1983; Frank et al., 1990; Portela et al., 2017). The literature review on the symmetric wake flows in this document focuses only on the rectangular cylinders, which is followed by a review of the literature on asymmetric wake flows.

2.1 Rectangular Cylinders in Uniform Flow

Separated flows over and behind sharp-edged square and rectangular cylinders have been studied extensively including the experimental investigations by Okajima (1982), Lyn et al. (1995), Moore et al. (2019a) and Kumahor and Tachie (2021), and numerical investigations by Franke et al. (1990), Bosch and Rodi (1998) and Trias et al. (2015). Moore et al. (2019a) investigate the Reynolds number effects on the reattachment location over an AR5 rectangular

cylinder using hot wire anemometry (HWA) and particle image velocimetry (PIV). They observed that the reattachment location shows a weak Reynolds number dependency at a sufficiently high value (Re > 50000). Meanwhile, important differences have been observed in the near wake region of the rectangular cylinders. The numerical investigation by Mashhadi et al. (2021) showed that the recirculation length, L_r, behind a square cylinder, increases linearly at low Reynolds numbers, 30 < Re < 200, reaching a maximum value of $L_r/h = 3.50$ at Re = 50 followed by a decrease to $L_r/h = 1.50$ at Re = 200 due to the transition from steady to unsteady flow. The flow characteristics in the wake region of a square cylinder were also experimentally studied by Sohankar (2006) and Bai and Alam (2018) at the Reynolds number range of 50 < Re < 45000 using HWA and PIV. They observed that the vortex formation length ($L_{u'}$), which is defined as the streamwise distance between the location of peak streamwise Reynolds normal stress and the trailing edge of the cylinder, reaches an asymptotic value of $L_{u'}$ = 0.54 at Re > 1000. However, this value is notably shorter than $L_{u'}/h$ = 0.8, observed over a square cylinder at Re = 3000 (Nakagawa et al., 1999). Using a PIV technique, Reynolds number effects on the separated flow induced by rectangular cylinders with AR = 0.5 (Kumahor and Tachie, 2023a) and AR = 1 and 4 (Liu et al., 2022a) were investigated at 3000 ≤ Re ≤ 21000. They reported that the wake vortex as well as the recirculation length and vortex formation length ($L_{v'}$), which is defined as the streamwise distance between the location of peak vertical Reynolds normal stress and the trailing edge of the cylinder, are largest at Re = 3000, and then decrease in size until a Reynolds number independency was reached at Re ≥ 14700. The asymptotic values of the recirculation and vortex formation lengths are $L_r/h = 0.45$, 0.54 and 0.72 and $L_{v'}/h = 0.45$, 1.07 and 1.79 for the AR0.5, AR1 and AR4 rectangular cases, respectively.

Previous investigations have also demonstrated that even though the separation points are fixed at the leading edge and flow properties asymptote at $Re \geq 14700$, the flow topology over and behind the rectangular cylinders can be significantly affected by the streamwise aspect ratio (Okajima, 1982; Nakagawa et al., 1999; Moore et al., 2019a; Liu et al., 2022b; Kumahor and Tachie, 2023b). For cylinders with a low aspect ratio ($AR < 2.5$), the separated shear layer emanating from the leading edge is shed directly into the wake region behind the cylinders so that the separated shear layer and the wake vortex are dynamically coupled (Okajima, 1982; Durao et al., 1988; Bosch and Rodi, 1998; Minguez et al., 2011; Portela et al., 2017; Moore et al., 2019a). For relatively larger aspect ratios of $AR > 3.5$, on the other hand, the separated shear layer reattaches on the cylinders, forming a primary vortex above the cylinder (Okajima, 1982; Kiya and Sasaki, 1983; Shimada and Ishihara, 2002; Bruno et al., 2014; Cimarelli et al., 2018; Moore et al., 2019a; Kumahor and Tachie, 2022). Under this condition, the flow separates again at the upper and lower trailing edges of the cylinder, forming two symmetric wake vortexes.

The effects of streamwise aspect ratio on the dynamics of the primary vortex above the cylinder and the wake vortex in the near wake region have been studied by many researchers (Nakagawa et al., 1999; Shadaram et al., 2008; Moore et al., 2019a; Kumahor and Tachie, 2022; Liu et al., 2022b). Kumahor and Tachie (2022), for example, investigated the streamwise aspect ratio effects on the separated shear layer induced by square (AR1) and AR5 cylinders using a planar PIV technique. They observed that the sizes of the primary and wake vortexes are smaller for the square cylinder compared to the AR5 rectangular cylinder. Furthermore, the maximum reverse flow velocities measured in the near wake region are the same for both cases, but the recovery of the mean flow is faster behind the square cylinder. Liu et al. (2022b) investigated the wake flow induced by AR1, AR2, AR3 and AR4 rectangular cylinders using PIV. They reported

that the AR2 cylinder features a distinctively larger wake vortex compared to the AR1, AR3, and AR4 cases, due to the intermittent reattachment of the separated shear layer on either the upper or the lower surfaces of the AR2 cylinder. The wake region behind rectangular cylinders was also studied by Nakagawa et al. (1999) using laser Doppler velocimetry (LDV), who reported that the large wake vortex produced by AR2 leads to comparably faster recovery of the mean streamwise velocity and longer recirculation and wake formation lengths compared to the AR0.5, AR1 and AR3 cases.

Table 1.1 provides a summary of selected past investigations of relevance to the present study. The table clearly shows that the streamwise aspect ratio has significant effects on the flow characteristics around the rectangular cylinders. For example, the investigation by Liu et al. (2022b) illustrated that the reattachment length on the rectangular cylinder increases as the aspect ratio increases. They reported that the mean reattachment length on the AR3 rectangular cylinder is L_T/h = 2.90 at *Re* = 7200, which is approximately 20% shorter than the reattachment length (L_T/h = 3.49) on the AR4 rectangular cylinder. A similar observation was also reported by Moore et al. (2019b) on the AR3 and AR5 rectangular cylinders. Meanwhile, aspect ratio effects were also observed in the wake region. Kumahor and Tachie (2022) reported that the recirculation length is L_r/h = 0.54 behind a square cylinder which is shorter than the recirculation length of L_r/h = 0.96 behind an AR5 rectangular cylinder. The vortex formation lengths are also significantly affected by the streamwise aspect ratio. At *Re* = 14700, Kumahor and Tachie (2023a) and Liu et al. (2023) reported that the vortex formation lengths are different behind AR0.5, AR1, AR2, AR3 and AR4 rectangular cylinders with $L_{v\prime}/h$ = 0.45, 1.07, 3.64, 1.30, and 1.79, respectively.

Significant scatter has also been observed in the Reynolds stresses, turbulent kinetic energy (TKE) and turbulent transport of TKE (Sohankar, 2006; Mohebi et al., 2017; Moore et al., 2019a;

Table 1.1: Summary of previous studies on rectangular cylinders.

Author	Measurement	*Re*	AR	L_T/h	L_r/h	$L_{u'}/h$	$L_{v'}/h$
Nakagawa et al. (1999)	HWA	3000	0.5	-	0.70	0.70	5.10
			1	-	0.60	0.80	6.20
			2	-	1.80	2.00	4.30
			3	-	0.90	1.00	4.20
Moore et al. (2019a)	PIV, HWA	50000	1	-	-	-	-
			3	2.80	-	-	-
			5	4.4	-	-	-
Kumahor and Tachie (2022)	PIV	16200	1	-	0.54	-	1.10
			5	4.30	0.96	-	2.20
Addai et al. (2022)	PIV	12750	1	-	0.57	-	0.95
Liu et al. (2022b)	PIV	7200	1	-	0.74	0.74	1.19
			2	-	3.10	3.48	4.29
			3	2.90	0.98	1.65	2.04
			4	3.49	0.96	2.15	2.59
Liu et al. (2023)	PIV	14700	1	-	0.54	0.60	1.07
			2	-	0.64	3.23	3.64
			3	2.85	0.62	0.83	1.30
			4	3.58	0.72	1.53	1.79
Kumahor and Tachie (2023a)	PIV	14700	0.5	-	0.45	-	0.45

Kumahor and Tachie, 2022; Liu et al., 2022b). It has been demonstrated that the dominant fluctuating velocity above the rectangular cylinder is the streamwise fluctuating velocity, while the vertical fluctuating velocity is dominant in the wake region behind the cylinder, resulting from the formation of von Kármán vortex street. However, differences in the magnitudes of Reynolds stresses occur due to variation in streamwise aspect ratios. Kumahor and Tachie (2022) reported that the Reynolds stresses are an order of magnitude higher for the square cylinder compared to the AR5 cylinder. Furthermore, unlike the AR5 rectangular cylinder, no distinct region of elevated vertical Reynolds stress is observed over the square cylinder. For the turbulent kinetic energy, it is observed that the TKE peak is located along the centerline in the wake region of square cylinder (Sahankar, 2006) and rectangular cylinders with $0.05 \leq AR \leq 1.92$ (Mohebi et al., 2017). Nevertheless, Kumahor and Tachie (2023b) observed that the TKE peaks in the wake of the AR4 cylinder occurred away from the centerline. Additionally, turbulent transport of TKE over the AR1, AR2, AR3 and AR4 rectangular cylinders by streamwise and vertical fluctuating velocities were analyzed by Liu et al. (2022b) using the third order moments. The topology of these third order moments shows low-speed ejection and high-speed sweep events, transporting fluid away and toward the cylinders, respectively. It is observed that the switch between ejection and sweep events occurs along the mean separating streamline emanating from the leading edge, regardless of the aspect ratio.

2.2 Asymmetric wake flows

The asymmetric wake flow has also been investigated in the past (Herry et al., 2011; Schewe, 2013; Moore et al., 2019a; Chalmers et al., 2022; Addai et al., 2022). For example, asymmetric wake flows behind a square cylinder placed in the vicinity of smooth and rough walls

were investigated by Shi et al. (2010), Chalmers et al. (2022) and Addai et al. (2022). Shi et al. (2010) observed that two asymmetric recirculation bubbles formed in the cylinder wake of gap ratio G/h = 0.4 and 0.8 (where G is the vertical offset distance from the bottom wall), but only a single recirculation bubble was formed at G/h = 0.1 and 0.2. As the gap distance changes, Chalmers et al. (2022) and Addai et al. (2022) reported significant changes in the levels of the streamwise Reynolds normal stress ($\overline{u'u'}$) in the upper and lower shear layers. Specifically, the magnitude of $\overline{u'u'}$ decreases as the gap ratio decreases and the peak magnitude in the lower shear layer is higher than that in the upper shear layer. They also observed that the maximum vertical Reynolds normal stress ($\overline{v'v'}$) is no longer located on the horizontal centerline of the cylinder due to the lack of symmetry.

The asymmetric wake flows produced by varying the angle of attack of rectangular cylinders were experimentally investigated by Nemes et al. (2012), Schewe (2013) and Moore et al. (2019b). They demonstrated that the behaviour of the separated flow induced by the rectangular cylinders can be significantly different on the upper and lower sides of the cylinder, when the symmetry is broken by changing the angle of attack, α. At high angles of attack ($\alpha > 4^o$), for instance, the unsteady load is no longer contributed equally from both sides of the cylinder, but mainly due to the shear layer on the pressure side. This results in a significant skewness of the PDF distribution of lift fluctuations at angles of attack $\alpha > 4^o$ compared to the Gaussian distribution observed at $\alpha = 0^o$ (Moore et al, 2019b). Schewe (2013) and Moore et al. (2019b) also observed discrepancy in the reattachment lengths on the upper and lower surfaces of both AR3 and AR5 rectangular cylinders at $\alpha > 4^o$, compared to AR3 and AR5 cylinders at $\alpha = 0^o$ for which the reattachment lengths on the upper and lower surfaces are the same.

Although previous studies have shown that the asymmetric wake flow can be induced by bluff bodies with asymmetric body geometries, the existing experimental (Herry et al., 2011; Rao et al., 2019; Kumahor and Tachie, 2022) and numerical investigations (Spalart et al., 1997; Kang, 2021) for such flows are limited compared to symmetric wake flow induced by bluff bodies with symmetric body geometries. Herry et al. (2011) and Rao et al. (2019), for example, investigated the flow around the double backward facing steps. They observed two asymmetric vortices behind the top step with a larger vortex on one side and a smaller elliptical-shaped vortex on the opposite side of the vertical midplane. Behind the bottom step, one of the vortices is closer to the base of the body and the other is farther away from the base. Asymmetric wake flow induced by the Ahmed body was numerically and experimentally investigated by Kang (2021) and Aleyasin et al. (2021), respectively. A pair of asymmetric recirculation bubbles form behind the body due to unequal strength of the downwash and upwash flows from the top and bottom sides of the body, respectively. Aleyasin et al (2021) also reported that the regions of elevated Reynolds stresses are larger in the upper shear layer compared to the lower shear layer. More recently, asymmetric wake flows induced by the asymmetric body geometry of bluff bodies in the form of the right-angled trapezoidal cylinder were investigated by Kumahor et al. (2022). They observed that the mean recirculation bubble over the AR1 trapezoidal cylinder is along the upper surface and extends into the wake region, which results in a larger recirculation region compared to the square cylinder.

2.3 Objectives

Despite the extensive literature on the flow dynamics around symmetric bluff bodies such as square and rectangular cylinders, research on the flow dynamics around asymmetric bluff bodies in uniform flow has not received significant attention. Therefore, the objectives of the present

study are: 1) to investigate the effects of streamwise aspect ratio on the characteristics of asymmetric wake flows induced by right-angled trapezoidal cylinders, and to compare these results with symmetric wake flows generated by rectangular cylinders of similar aspect ratios; 2) to provide comprehensive benchmark datasets that will guide the development and of future numerical results.

To achieve these objectives, experiments were performed using trapezoidal cylinders with AR = 1, 2, 3, 4 and 5. According to Liu et al. (2022a) and Kumahor and Tachie (2023a), who investigated wake characteristics of rectangular cylinders over the AR range of $1 \leq AR \leq 5$ and Reynolds number range of $3000 \leq Re \leq 21000$ in the same test facility as in the present study, the wake flow characteristics are independent of Reynolds number for $Re \geq 14700$. Therefore, the experiments were performed at a Reynolds number of 14700. The velocity measurements were performed using a planar particle image velocimetry, and the results are discussed in terms of the mean flow, Reynolds stresses, turbulent kinetic energy (TKE) and its transport and production, probability density function (PDF) and joint probability density function (JPDF), and two-point autocorrelations.

3. EXPERIMENTAL SET-UP AND MEASUREMENT PROCEDURE

This chapter presents the experimental set-up and measurement procedure employed to obtain the velocity data. Specifically, a description of the test facility, the particle image velocimetry system as well as a summary of the test cases and measurement procedures are included in this chapter. Also, measurement uncertainty analysis is provided at the end of this chapter.

3.1 Test Facility

The experiments were conducted in a recirculating open water channel located in the Turbulence and Hydraulic Engineering Laboratory (THEL) at the University of Manitoba. A picture of the water channel facility is shown in Figure 3.1. The length of the open water channel

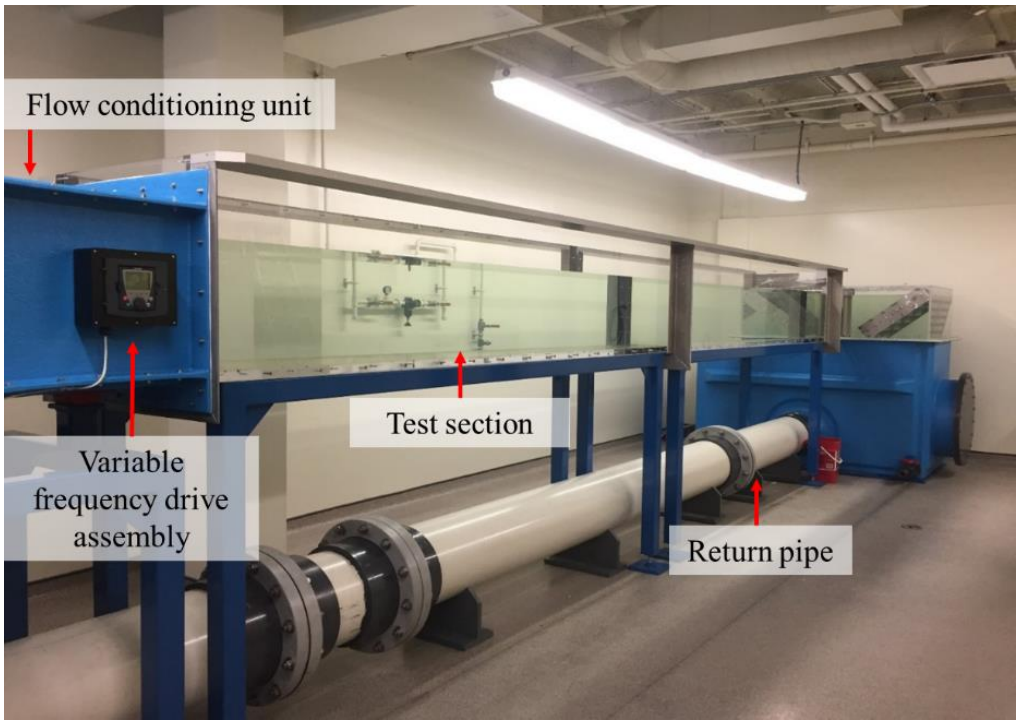

Figure 3.1: A picture of the open recirculating water channel showing the various components of the facility.

system is 12.00 m. The system includes a flow conditioning unit, a test section and a return plenum. The flow conditioning unit consists of a perforated plate, a hexagonal honeycomb, and mesh screens of various sizes and a 4.88:1 converging section, which is employed to reduce the turbulent motion, and make the flow uniform before entering the test section. The dimension of the test section is 6.00 m long × 0.60 m wide × 0.45 m high. To facilitate optical access to flow, the side and bottom walls of the test section were manufactured from a 31.8 mm thick transparent Super Abrasion Resistant® (SAR) acrylic plate. The water flow is driven by a 40 HP variable-speed motor which controls the flow velocity from 0.03 m/s up to 2.0 m/s.

3.2 Particle Image Velocimetry System

The particle image velocimetry (PIV) system includes three 12-bit complementary metal oxide semiconductor (CMOS) cameras, a diode pumped dual-cavity high-speed Neodymium-doped yttrium lithium fluoride (Nd:YLF) laser and a computer equipped with the data acquisition and post-processing software. Figure 3.2 shows a picture of the PIV system with two high-speed side-by-side COMS cameras mounted on a transverse system. Also shown is the Nd: YLF laser placed above the water channel. The Nd: YLF laser is employed to illuminate the seeding particles by emitting the green laser light of wavelength 527 nm at a maximum pulse energy of 30 mJ/pulse per cavity. The illuminated particles are then captured by the CMOS cameras which have a full resolution of 2560 pixel × 1600 pixel and are able to achieve the image acquisition rates up to 807 Hz. Higher image acquisition rates up to 10 kHz can also be achieved but the resolution of the camera needs to be reduced. A commercial software, DaVis supplied by LaVision Inc., is used to perform the data acquisition, image-processing and vector calculations.

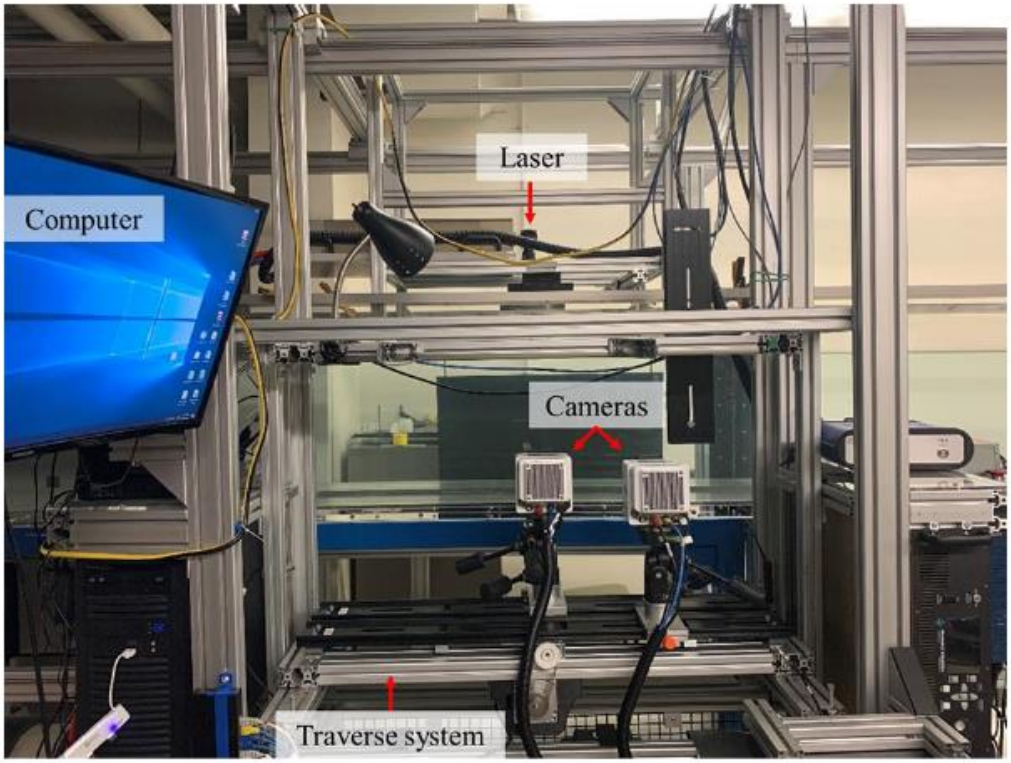

Figure 3.2: A picture of the particle image velocimetry (PIV) system.

3.3 Test Cases and Measurement Procedures

The schematics of the front and side views of the experimental set-up for the present study are shown in Figure 3.3. The test cylinders were machined from a smooth acrylic plate with a constant vertical height of $h = 0.03$ m and spanwise width of $w = 0.588$ m. Right-angled trapezoidal cylinders with an angle, $\alpha = 45°$, fixed bottom length $L_1 = 0.03$ m and various lower lengths, $L = 0.03$ m, 0.06 m, 0.09 m, 0.12 m, and 0.15 m corresponding to streamwise aspect ratios of AR $(= L/h) = 1, 2, 3, 4$ and 5, respectively, were mounted in position between two 6-mm thick acrylic plates that were clamped to the sidewalls of the test section. The origin of the Cartesian coordinate system, marked as *O*, with x and y representing the streamwise and vertical directions, respectively, is located at the right upper corner of the cylinder. The water depth in the channel

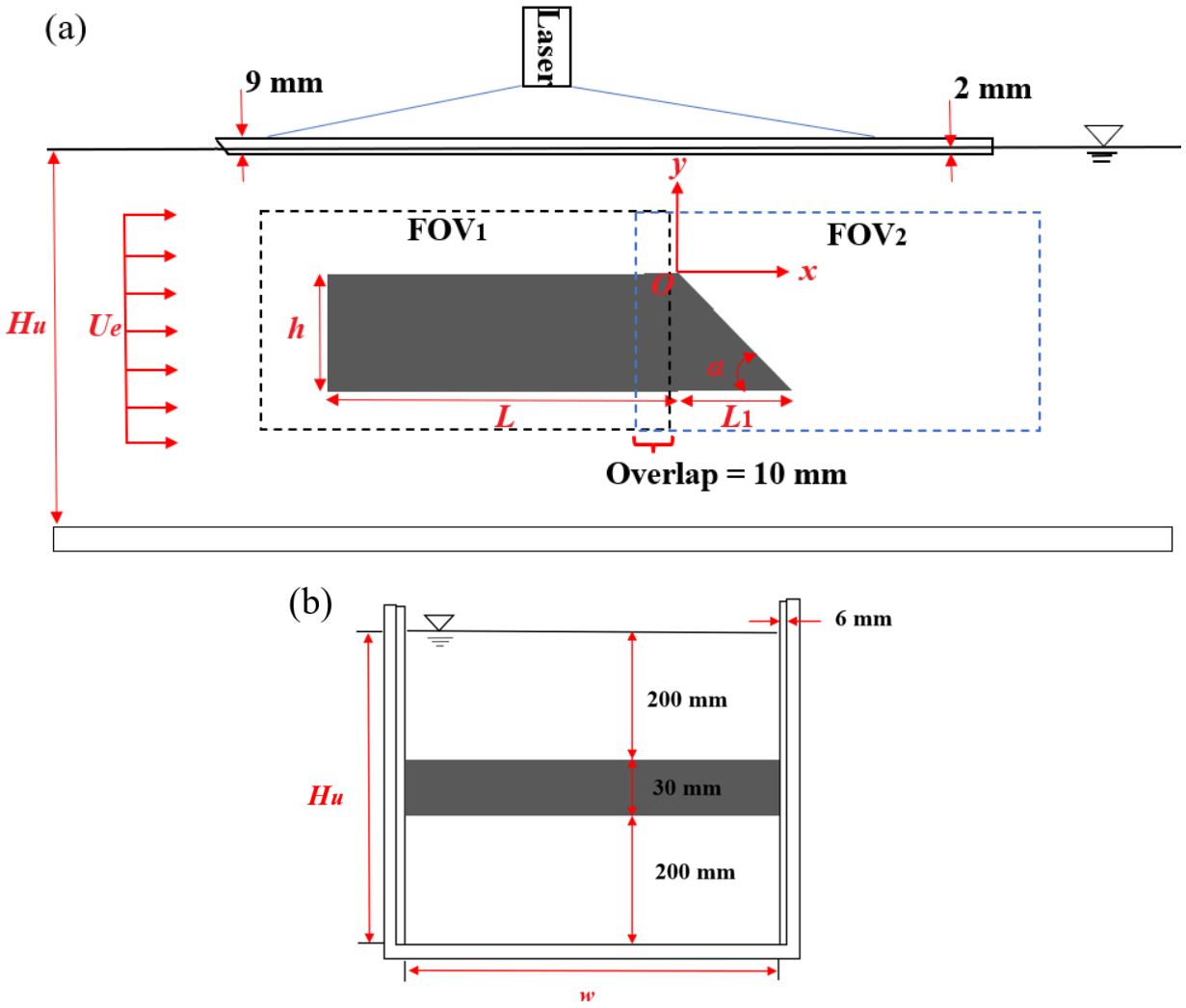

Figure 3.3: Schematics (not to scale) of the side view (a) and front view (b) of the experimental set-up for the current study.

was maintained at $H_u = 0.43$ m, as such the blockage ratio was BR $(= h/H_u) = 7\%$. According to Fang and Tachie (2019), the side-wall effects at channel mid-span are negligible when $w/h > 12$. The spanwise ratio in the present study was $w/h = 19.6$ and is deemed sufficient to minimize side-wall effects on the results. The free-stream velocity was set to $U_e = 0.49$ m/s and the kinematic viscosity of the water flow was $\nu = 10^{-6}$ m^2/s, at a room temperature of 20°C. The Reynolds number was $Re = 14700$. Meanwhile, the Froude number was Fr $(= U_e/\sqrt{gH_u}) =$

0.24, where $g = 9.81$ m/s is the acceleration due to gravity, which implies that the free surface had negligible influence on the flow dynamics over the cylinder. The free-stream turbulent intensity was $Tu = \sqrt{\overline{u'u'}}/U_e \approx 1\%$ for all test cases.

Two-component velocity measurements were performed in the $x - y$ plane at the channel mid-span, using a planar particle image velocimetry (PIV) technique. The seeding particles used in the experiments are silver-coated hollow glass spheres with a mean diameter of 10 μm and specific gravity of 1.4. Following Raffel et al. (2007), the slip velocity (U_s) of the seeding particle was 2.18 × 10^{-5} m/s and the relaxation time (τ_p) was 2.2 × 10^{-6} s, using equations (1) and (2), respectively.

$$U_s = \frac{{d_p}^2(\rho_p - \rho_f)g}{18\rho_f \nu} \tag{1}$$

$$\tau_p = \frac{{d_p}^2(\rho_p - \rho_f)}{18\rho_f \nu} \tag{2}$$

where $\rho_p = 1.4$ g/cm^3 and $\rho_f = 1$ g/cm^3 are the density of the seeding particle and the density of water, respectively. The characteristic time scale, $\tau_f (= \frac{h}{U_e}) = 6.1 \times 10^{-2}$ s, and the Stokes number, $S_k (= \frac{\tau_p}{\tau_f}) = 0.000036$. Since the value of S_k is within the recommended range of $S_k \leq 0.05$ (Samimy et al., 1991), the seeding particles are assumed to follow the fluid motions faithfully.

The seeding particles were illuminated using a diode-pumped dual-cavity, high-speed Neodymium-doped yttrium lithium fluoride (Nd: YLF) laser with a maximum pulse energy of 30 mJ/pulse per cavity. The wavelength of the laser is 527 nm. A transparent acrylic plate with a thickness of 9 mm and streamwise length of 0.60 m spanning the entire width of the test section was submerged 2 mm into the water to minimize the distortion of the laser light by the free surface,

as shown in Figure 3.3. Ebenezer et al. (2021) investigated the effect of the same plate on the wake flow generated by circular cylinders and observed no flow separation. Their results showed that the boundary layer thickness formed on the plate is very thin ($\delta_p = 6.5$ mm, where δ_p is based on the wall-normal location of $0.99U_e$ from the plate) and that the plate has no significant influence on the wake flow. The illuminated seeding particles were imaged by two side-by-side high-speed 12-bit Phantom VEO340L complementary metal-oxide-semiconductor (CMOS) cameras with a resolution of 2560 pixels × 1600 pixels. The dimensions of the fields of view (FOV) of these two cameras were: $\text{FOV}_1 = \text{FOV}_2 = 218.50$ mm × 136.60 mm. Also, there was a 10 mm overlap between the two fields of view in the streamwise direction. 12000 statistically independent image pairs were collected per field of view at a sampling frequency of 3 Hz. The data acquisition, image processing, and velocity vector calculation were performed using commercial software, DaVis Version 10.0.5, supplied by LaVision Inc. (Ypsilanti, Michigan, United States of America). An interrogation area (IA) of 64 pixels × 64 pixels with 50% overlap was used as a first pass followed by four final passes with 24 pixels × 24 pixels with 75% overlap.

3.4 Measurement Uncertainty

Following Bendat and Piersol (2010), Ebenezer et al. (2015) and Sciacchitano and Wieneke (2016), the measurement uncertainties in the streamwise mean velocity (ξ_U), Reynolds normal stresses ($\xi_{u_iu_i}$) and Reynolds shear stress (ξ_{uv}) were quantified using the following equations:

$$\xi_U = \frac{Z_c}{\sqrt{N}} \frac{u_{rms}}{U} \tag{3}$$

$$\xi_{u_iu_i} = Z_c \sqrt{\frac{1}{N}\left(\frac{\overline{u_i'u_i'u_i'u_i'}}{\left(\overline{u_i'u_i'}\right)^2} - 1\right)} \tag{4}$$

$$\xi_{uv} = Z_c\sqrt{\frac{1+\rho_{uv}^2}{N-1}} \tag{5}$$

In equation (5), $\rho_{uv} = \frac{\overline{u'v'}}{u_{rms}\times v_{rms}}$, is the cross-correlation coefficient between u', and v'. Since the samples are uncorrelated, the effective number of samples is equal to the total sample size, $N = 12000$. A confidence coefficient, $Z_c = 1.96$, is applied to qualify the measurement uncertainty within 95% confident level (Sciacchitano et al., 2016). In the present study, the measurement uncertainties in the mean streamwise velocity and Reynolds stresses were 0.1% and 1.8%, respectively, in the uniform flow. The uncertainty in the mean velocity increased to 3.2% along the shear layer and in the wake region due to the local turbulent levels in those regions, while the maximum uncertainties in the Reynolds normal and shear stresses were 5.0% and 2.2%, respectively. Since the level of uncertainty is not the same through the separated shear layer, the distributions of uncertainties in the streamwise mean velocity, Reynolds normal stresses and Reynolds shear stress for the AR1 and AR3 cases are shown as examples in A.1 in the appendix.

4. RESULTS AND DISCUSSION

This chapter presents the discussion of the findings of the present study. The discussion is based on the published journal paper: Kang, J., and Tachie, M. F., 2023, "Experimental Study of Turbulent Wake Flow Around Trapezoidal Cylinders with Varying Streamwise Aspect Ratios," Journal of Fluid Engineering, 1-49. DOI: 10.1115/1.4062086.

The results and discussion in this chapter are categorized as follows: In Section 4.1, the topological similarities and differences in the mean flow field among the various streamwise aspect ratios are examined. The analysis of the Reynolds stresses and turbulent kinetic energy (TKE) are presented in Section 4.2, and the turbulent transport and production term of TKE are analyzed in Section 4.3. In Section 4.4, one-dimensional profiles at some selected locations are examined while the probability density function (PDF) and joint probability density function (JPDF) are used to examine the characteristics of the asymmetric wake flow in Section 4.5. The effects of aspect ratio on the large-scale structures over and behind the cylinder are discussed in terms of two-point autocorrelations in Section 4.6.

4.1 Mean Flow Characteristics

Figure 4.1 shows contours of the streamwise mean velocity (U) and vertical mean velocity (V). Since the laser was shot from the top, the region beneath the cylinders could not be imaged due to the shadow cast by the cylinders and have been zeroed out in all the contours. The mean flow separates at the leading edge, irrespective of the aspect ratio, and accelerates past the cylinder. The mean streamlines (continuous lines) show that the separated shear layer forms a recirculation

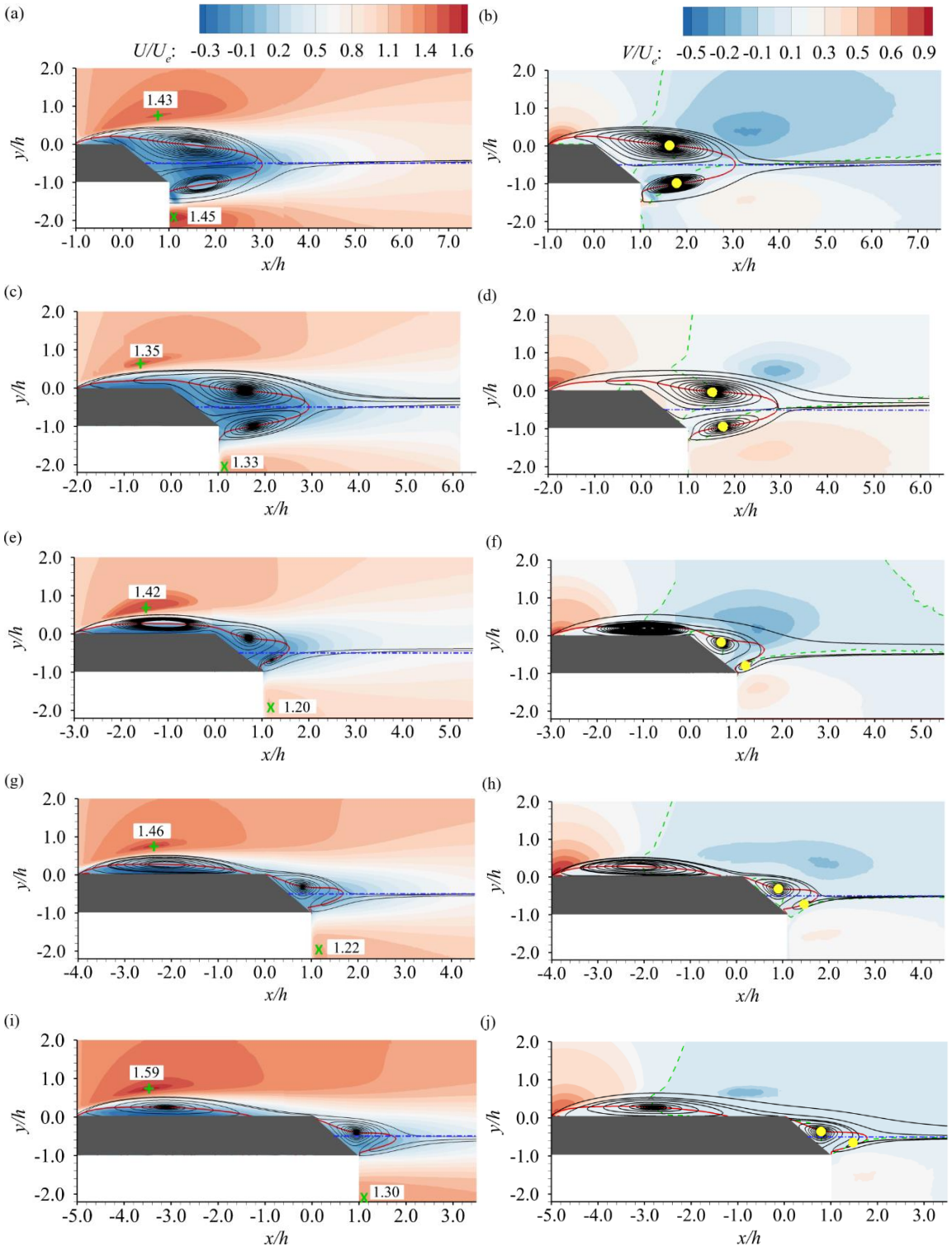

Figure 4.1: Contours of streamwise mean velocity (U) and vertical mean velocity (V), superimposed with mean streamlines (continuous lines), the isopleth of $U = 0$ (thick solid line) and the horizontal centerline of the cylinder (dashed line). The additional dashed line in the V contour is the isopleth of $V = 0$. Symbols of $+$ and $\times$ represent the local peaks over the cylinder and in the near wake region, respectively.

bubble which is confined to the surface of the longer cylinders (AR3, AR4 and AR5) but extends into the wake region in the AR1 and AR2 cases. This recirculation bubble is hereafter referred to as the primary vortex. In the case of the AR1 and AR2 rectangular cylinders, the separated shear layer forms a primary vortex above the cylinder and then descends into the near wake region, forming a recirculation bubble in the wake behind the trailing edge, which is referred to as the wake vortex (Cimarelli et al., 2018; Kumahor and Tachie, 2022; Liu et al., 2022b). Due to the modified trailing edge in the present study, the reversing flow in the near wake region is redirected along the inclined surface of the AR1 and AR2 trapezoidal cases towards the upper surface of the cylinder. Therefore, the primary vortex and the wake vortex in the AR1 and AR2 cases are merged into a massive vortex behind the trailing edge. Additionally, a distinct but smaller vortex is observed in the lower shear layer of the AR1 and AR2 trapezoidal cases. As the streamwise extent of the cylinder increases, two wake vortexes are formed in the near wake region of the longer cylinders and are increasingly asymmetric about the horizontal centerline of the cylinder (dashed line). Specifically, the lower vortex diminishes in comparison to the upper vortex in the AR3 case and tends to disappear at the largest aspect ratios (AR4 and AR5). These two wake vortexes were also observed in the AR3, AR4 and AR5 rectangular cases (Bruno et al., 2014; Guissart et al., 2019; Moore et al., 2019a; Moore et al., 2019b; Kumahor and Tachie, 2022; Liu et al., 2022a), but they are symmetric about the horizontal centerline due to the symmetric body geometry of the rectangular cylinders.

The isopleth of $U = 0$ (thick solid line), which is used to determine the mean reattachment point (i.e. the streamwise location where $U = 0$ isopleth intersects with the top surface of the cylinder), shows that the mean flow reattaches on the surface of AR4 and AR5 cylinders, but no mean reattachment occurs over the AR1, AR2 and AR3 cylinders. The reattachment length,

defined as the streamwise distance from the leading edge to the reattachment point, is 3.70h and 3.79h, respectively, in the AR4 and AR5 cases. The former is in good agreement with a reattachment length of 3.60h reported for an AR4 rectangular cylinder at the same Reynolds number (Liu at al., 2022b). The latter is also in good agreement with 3.65h reported by Cimarelli et al. (2018) for an AR5 rectangular case at $Re = 3000$ but is shorter than the value of 4.30h reported by Kumahor and Tachie (2022) at $Re = 16200$. Additionally, the maximum streamwise mean velocity (U) shown in Figures 4.1(a, c, e, g, i) is observed along the upper shear layer and prior to the trailing edge of the cylinders, except in the AR1 case. In the lower shear layer, another distinct positive peak occurred close to the lower trailing edge. This peak has a similar value as the maximum U above the cylinder in the AR1 and AR2 cases but is comparatively smaller in the longer cases.

In Figures 4.1(b, d, f, h, j), identical positive V peak region is observed upstream of the cylinder, regardless of the aspect ratio, due to the same front face and separation point. Downstream the leading edge, the mean vertical velocity switches sign from positive to negative on the upper surface of the longer cases (AR3, AR4 and AR5) but it occurs on the inclined surface of the AR1 and AR2 cases. The negative V region is associated with the entrainment of the free-stream fluid into the mean recirculation bubbles, enhancing mixing in the wake flows (Addai et al., 2022). The delayed sign switch in the AR1 and AR2 cases is due to the massive primary vortex behind the cylinder, which indicates the more significant downward deflection of the mean flow from the upper surface of the AR1 and AR2 cases compared to the longer cases. It is also expected that the larger wake vortex close to the upper trialing edge of the longer cylinders (AR3, AR4 and AR5) could be associated to the stronger downward deflection of the mean flow due to the modified upper trailing edge.

Figure 4.2 compares the contours of the mean spanwise vorticity ($\omega_z = \partial V/\partial x - \partial U/\partial y$), superimposed with the isopleth of $U = 0$. Figures (b), (d), (f), (h) and (j) show the contour of mean spanwise vorticity, superimposed with mean velocity vector plots around the upper trailing edge of the cylinder. It is observed that the spanwise vorticity is concentrated at the leading edge of the cylinder and diffuses as the streamwise distance increases, regardless of the aspect ratio (Moore et al., 2019a; Addai et al., 2022). Above the upper trailing edge, the vorticity contours clearly show which of those test cases experience mean reattachment by the occurrence of distinct positive and negative ω_z regions. Specifically, the positive ω_z region results from the flow close to the upper surface separating off the upper trailing edge corner of the shorter cylinders before flowing upstream. As depicted in Figures (b), (d), (f), (h) and (j), the vector plots show that part of the mean recirculating flow in the near wake region of the cylinders is redirected upstream along the inclined surface and onto the upper surface of the cylinder for AR1, AR2 and AR3. However, no such observation is made for the AR4 and AR5. Additionally, two ω_z peaks are observed. The magnitude of the upper peak near the leading edge of the cylinder is significantly larger compared to the lower peak, irrespective of the aspect ratio. This is due to the strong mean shear ($\partial U/\partial y$) associated with the flow at the leading edge of the cylinder (Addai et al., 2022). In the wake region, the lower peak is located near the lower trailing edge of the cylinder. It is noteworthy that the largest magnitude of the lower peak is observed in the AR1 case.

To further assess the effects of streamwise aspect ratio and body geometry on the mean flow topology, metrics such as the maximum streamwise mean velocity (U_{max}), maximum backflow velocity (U_b), reattachment possibility on the top surface of the cylinders and the upper and lower vortex core locations in the wake region, are examined in Figure 4.3. The data for rectangular cylinders reported in previous studies (Trias et al., 2015; Kumahor and Tachie, 2022;

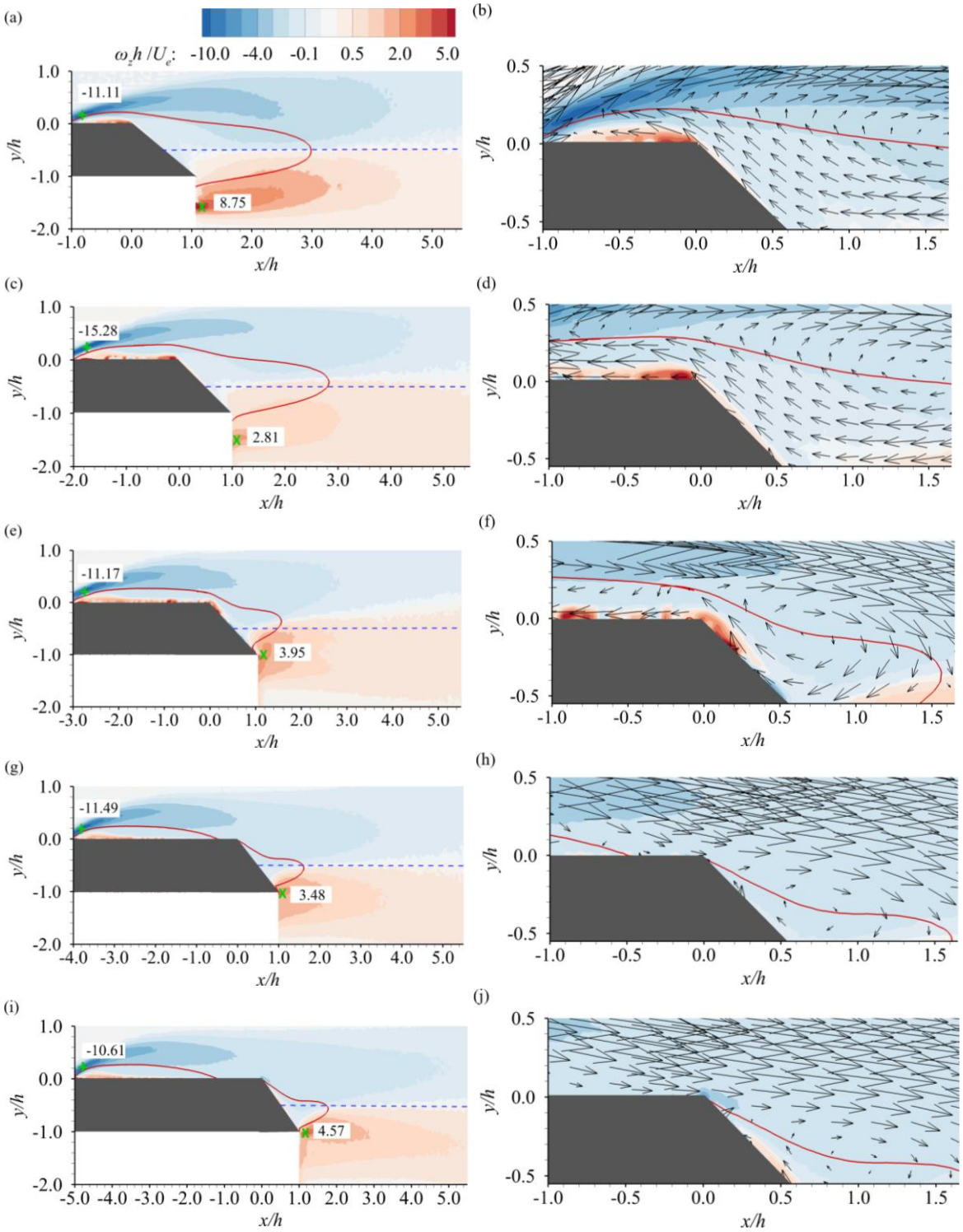

Figure 4.2: Contours of spanwise vorticity (ω_z), superimposed with the isopleth of $U = 0$ (solid line) and the horizontal centerline of the cylinder (dashed line). Figures (b), (d), (f), (h) and (j) show the ω_z contours and the superimposed mean velocity vectors around the upper trailing edge of the cylinder. Symbols of + and × represent the local peaks over the cylinder and in the near wake region, respectively.

Liu et al., 2023) are included for comparison. From Figure 4.3(a), the distribution shows that U_{max} drops from $1.43U_e$ (AR1 case) to $1.35U_e$ (AR2 case) and then increases monotonically to $1.59U_e$ (AR5 case). In the range of AR $\geq$ 2, the distribution of U_{max} is approximately given by the function, $U_{max}/U_e = 0.076\text{AR} + 1.19$, as shown by the dashed line in Figure 4.3(a). The U_{max} for the trapezoidal case is smaller than those for the rectangular cylinders with AR = 1 and 2 but is nearly the same for AR = 3 and larger for the AR4 and AR5 cylinders. It is also noted that, for both trapezoidal and rectangular cylinders, U_{max} is lowest at AR = 2. In Figure 4.3(b), the magnitude of U_b decreases linearly for AR $\leq$ 4, and then reaches an asymptotic value of $-0.11U_e$, at AR = 4 and 5. The linear region follows the correlation: $U_b/U_e = 0.067\text{AR} - 0.38$. According to Kumahor and Tachie (2022), the largest magnitude of reverse flow in the AR1 case is the reason for the formation of the largest wake region behind the AR1 cylinder, as shown in Figure 4.1(a). In comparison to rectangular cylinders, notable differences are observed at AR $\leq$ 3, where the magnitudes of the maximum backflow velocities are larger in AR1 and AR3 trapezoidal cases but are similar in the AR2 trapezoidal and rectangular cases, at approximately $0.23U_e$. For the larger aspect ratios, the maximum backflow reaches asymptotic value of $0.12U_e \pm 0.01U_e$.

The reattachment possibility of the test case is determined by the isopleths of forward flow fraction originating from the leading edge and terminating at the trailing edge of the cylinder (Kumahor and Tachie, 2022). Figure 4.3(c) shows that the reattachment possibility can be significantly affected by both aspect ratio and geometry of the cylinder. For trapezoidal cylinders, the AR1 and AR2 cases have similar and smaller reattachment possibilities (6%) compared to the cases with larger aspect ratios. As the aspect ratios increase from 2 to 5, the reattachment possibility increases linearly to 90% as follows: Reattachment Possibility = 29.02AR – 51.87. The

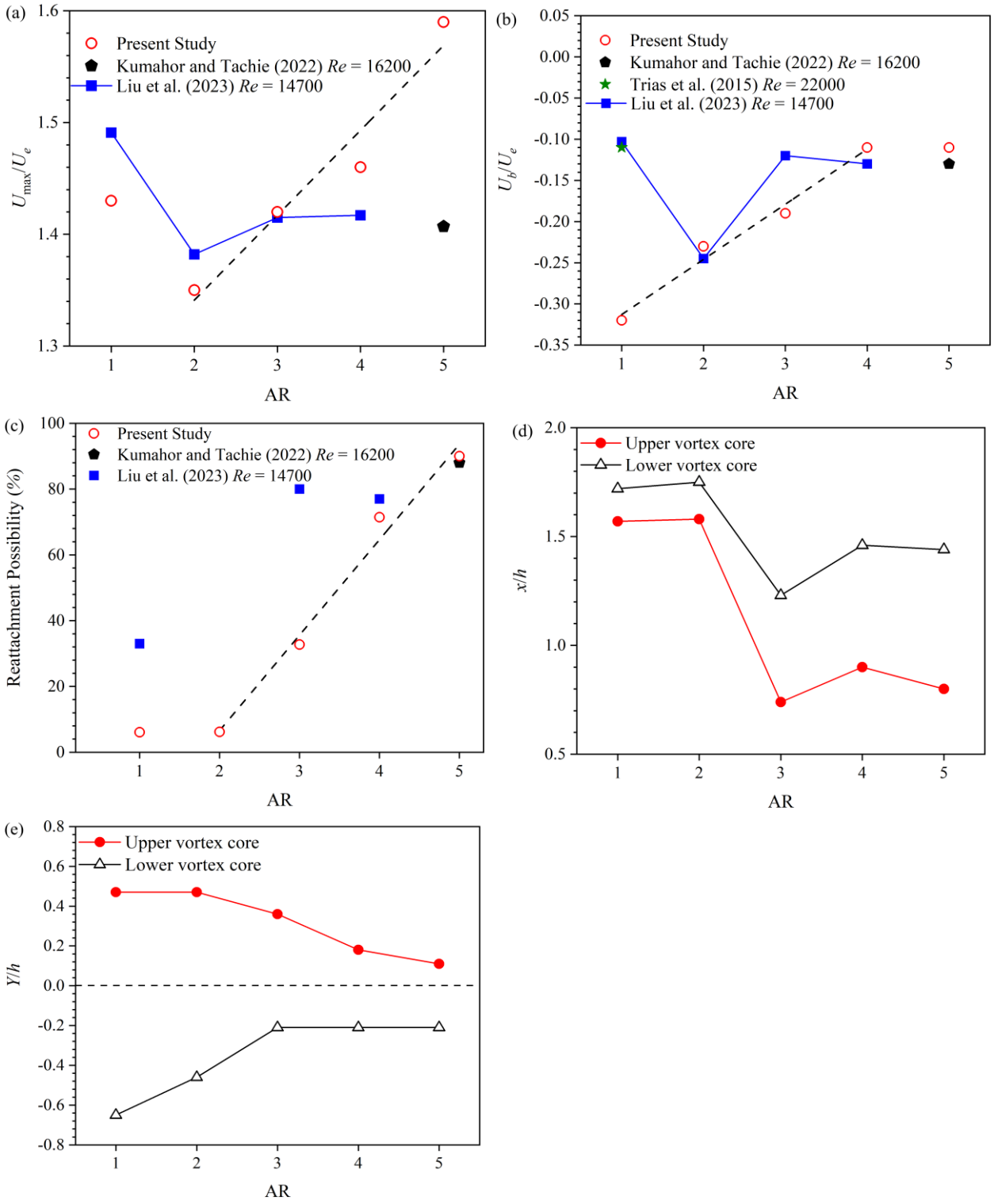

Figure 4.3: Distributions of maximum streamwise mean velocity (U_{max}) in the upper shear layer, (a), maximum backflow velocity (U_b), (b), reattachment possibility, (c), and x/h and Y/h locations of the upper and lower vortex cores in the wake region, (d) and (e), respectively.

marked increase from AR2 to AR5 is a reflection of significant flow differences induced by the aspect ratio changes. Compared to rectangular cases, the reattachment possibilities for the AR1 and AR3 trapezoidal cases (6% and 32%) are considerably smaller than the corresponding values for the AR1 and AR3 rectangular cases (33% and 81%), respectively. The reason can be related to part of the mean recirculating flow in the near wake region of the AR1 and AR3 trapezoidal cylinders flowing back to the upper surface along the inclined surface. However, the reattachment possibilities of the AR4 and AR5 trapezoidal cases (72% and 90%) are in good agreement with the values of 77% and 88%, respectively, for the AR4 and AR5 rectangular cases. These results demonstrate that the modified trailing surface of the trapezoidal cylinder has less effect on flow reattachment in the AR4 and AR5 cases, as the wake region is increasingly further away from the point of flow separation, i.e. the leading edge of the cylinder.

Following Lyn et al. (1995), Moore et al. (2019a) and Addai et al. (2022), the vortex cores are determined as the intersection of the isopleths of $U = 0$ and $V = 0$. Figures 4.3(d-e) show the distributions of the streamwise location (x/h) of the vortex cores in the near wake region relative to the trailing edge of the cylinder, and the vertical distances (Y/h), relative to the horizontal centerline. Figure 4.3(d) shows that the upper vortex core is closer to the origin (trailing edge) compared to the lower vortex core, irrespective of the aspect ratio. The x locations of both the upper and lower vortex cores at AR = 1 and 2 are farther away from the trailing edge compared to the larger aspect ratios. Additionally, the furthest and nearest x locations, with respect to the trailing edge, of both the upper and lower vortex cores are observed at AR = 2 and AR = 3, respectively. The farthest x location of the vortex core in the near wake region of rectangular cylinders with the same aspect ratios (AR = 1, 2, 3, 4 and 5) was also observed in the AR2 case due to the quasi-periodic attachment and detachment over the AR2 rectangular cylinder surface

(Okajima, 1982; Nakagawa et al., 1999). In Figure 4.3(e), the distribution shows that the Y location of the upper vortex core decreases from $0.47h$ to $0.11h$ as the aspect ratio increases, approaching $Y/h = 0$, (horizontal centerline of the cylinder). However, the Y location of the lower vortex core from the centerline decreased from $0.65h$ at AR $= 1$ to an asymptotic value of $0.21h \pm 0.01h$ at AR ≥ 3. The furthest x/h and Y/h locations of the wake vortex in the AR1 and AR2 cases indicate larger recirculation regions are formed behind these cases compared to the larger aspect ratio cases (Kumahor and Tachie, 2023a), which is consistent with the observations in Figures 4.1 and 4.3(b).

4.2 Reynolds Stresses and Turbulent Kinetic Energy

The distributions of Reynolds stresses and TKE are presented to examine the effects of aspect ratios on the second-order moments. Figure 4.4 shows contours of streamwise Reynolds normal stresses ($\overline{u'u'}$) and vertical Reynolds normal stress ($\overline{v'v'}$). Elevated regions of the Reynolds normal stresses are aligned along the mean separating streamline (continuous line) starting from the leading edge and are more elongated as the aspect ratio increases. The strongest velocity fluctuation associated with the separated shear layer over the cylinder is the streamwise Reynolds stress ($\overline{u'u'}$) which peaks above the cylinders, except in the AR1 case. Similar $\overline{u'u'}$ peaks were also observed above rectangular cylinders with AR $= 1$, 2, 3, 4 and 5 (Nakagawa et al., 1999; Chang et al., 2022; Liu et al., 2022b). In the near wake region, dual $\overline{u'u'}$ peaks are observed and distributed asymmetrically about the horizontal centerline due to the asymmetric body geometry of the trapezoidal cylinder. These dual $\overline{u'u'}$ peaks were also reported by Kumahor and Tachie (2022) and Liu et al. (2022a) in the near wake region of a rectangular cylinder but they are

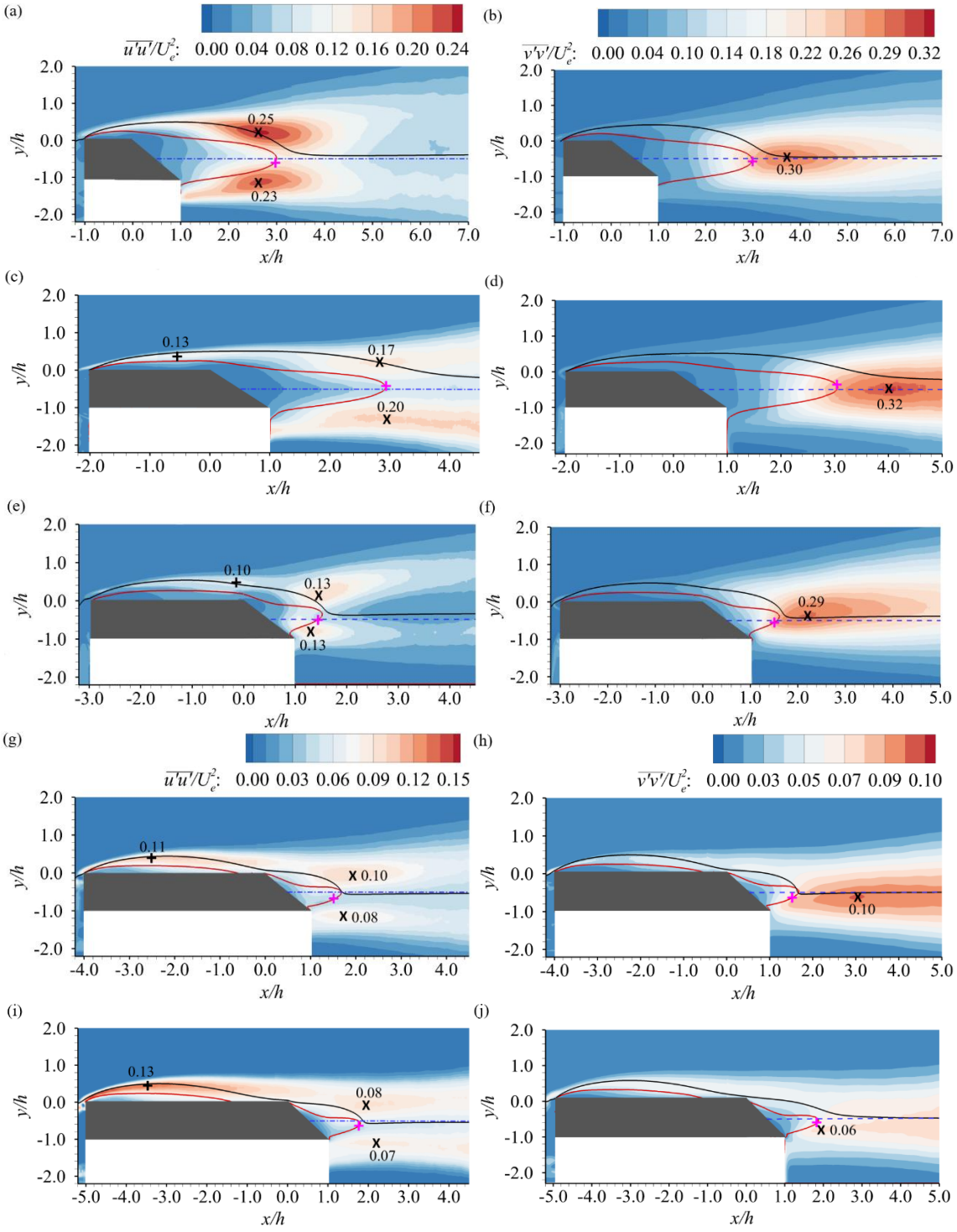

Figure 4.4: Contours of streamwise Reynolds normal stress ($\overline{u'u'}$) (a), (c), (e), (g) and (i), and vertical Reynolds normal stress ($\overline{v'v'}$) (b), (d), (f), (h) and (j) superimposed with mean separating streamlines (continuous line), the isopleth of $U = 0$ (solid line) and the horizontal centerline of the cylinder (dashed line). The + symbol in the near wake region represents the rear stagnation point of the recirculation region. Symbols of + and × over and behind the cylinder, respectively, represent the local peaks.

symmetric about the horizontal centerline. Similar to the rectangular cases (Guissart et al., 2019), the elevated $\overline{v'v'}$ peak regions of the trapezoidal cases occur along the horizontal centerline in the near wake region of the cylinder. According to Nakagawa et al. (1999) and Liu et al. (2022a), this elevated $\overline{v'v'}$ region is associated with the alternate shedding of vortices from both the upper and lower surfaces of the cylinder. The rear stagnation point of the recirculation region behind the cylinder is characterized by the intersection of streamlines (Lyn et al., 1995) and is marked by the '+' symbol in Figure 4.4. Similar to the rectangular cases (Durao et al., 1988; Lyn et al., 1995; Nakagawa et al., 1999), the $\overline{u'u'}$ and $\overline{v'v'}$ peaks in the wake region are close to this rear stagnation point.

Contours of the Reynolds shear stress ($\overline{u'v'}$) and TKE are shown in Figure 4.5. Since the spanwise velocity was not measured, the turbulent kinetic energy was estimated as follows: TKE = 0.5 ($\overline{u'u'} + \overline{v'v'}$). Due to the misalignment of the Cartesian coordinate with the local mean streamlines (Kiya and Sasaki, 1983), a distinct positive $\overline{u'v'}$ region is evident close to the leading edge, regardless of the aspect ratios. The same observation was also reported in previous investigations on rectangular cylinders in uniform flow (Kumahor et al., 2021) as well as wall-mounted bluff bodies (Kumahor et al., 2021; Chalmers et al., 2022). Around the trailing surface, the negative $\overline{u'v'}$ region is more dominant than the positive $\overline{u'v'}$ region in all case, except for a small positive $\overline{u'v'}$ region near the upper trailing edge of the AR2 cylinder. In the wake region, the isopleth of $\overline{u'v'} = 0$ moves upwards and eventually overlaps with the horizontal centerline of the cylinder. Additionally, two $\overline{u'v'}$ peaks appear and are asymmetric about the horizontal centerline of the cylinder. The magnitudes of the $\overline{u'v'}$ peaks are larger in the AR1, AR2 and AR3 cases compared to the peaks in the AR4 and AR5 cases. Also, the magnitude of $\overline{u'v'}$ peak in the

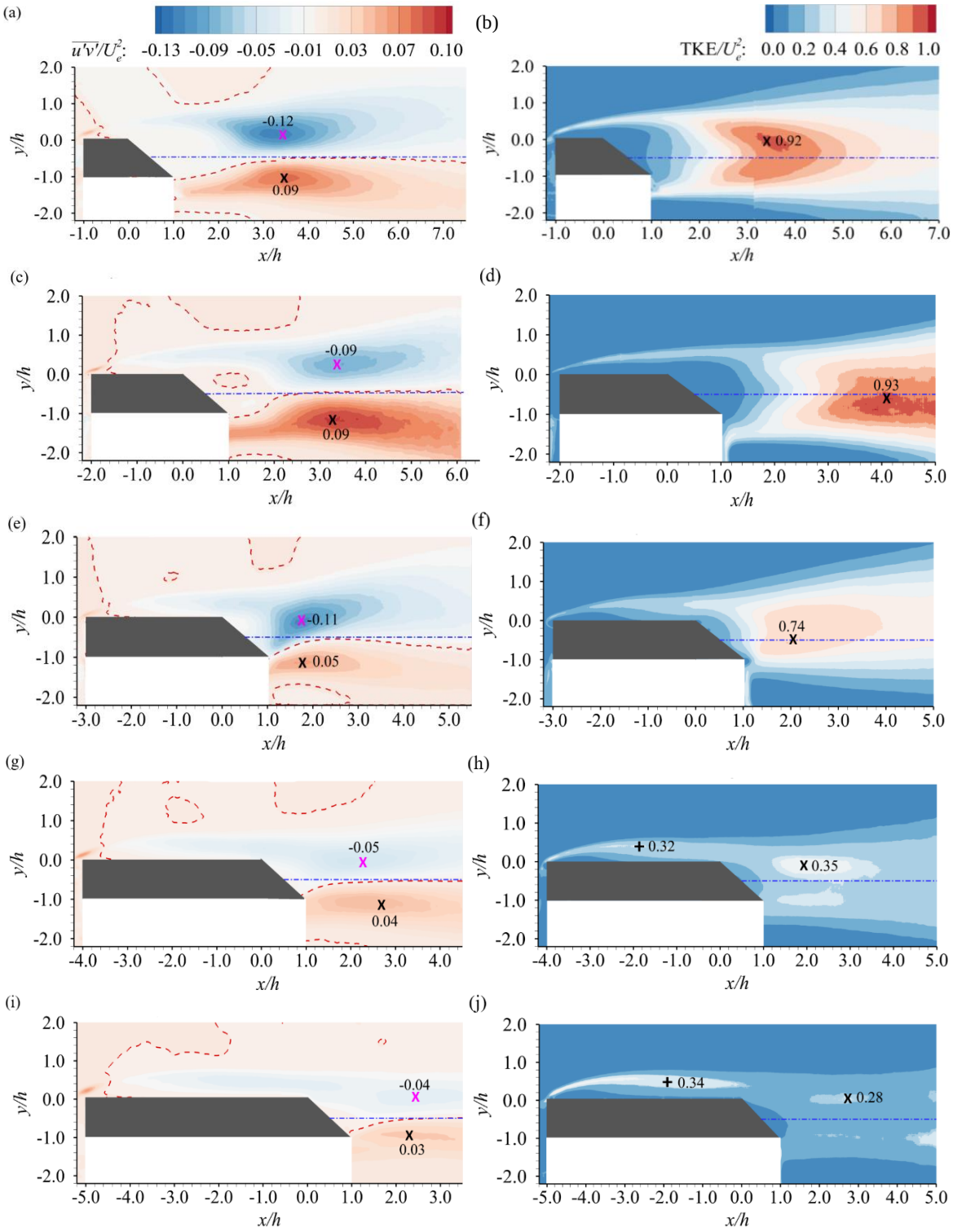

Figure 4.5: Contours of Reynolds shear stress ($\overline{u'v'}$), (a), (c), (e), (g) and (i), and turbulent kinetic energy (TKE), (b), (d), (f), (h) and (j) superimposed with the horizontal centerline of the cylinder (dashed line). The additional dashed line in $\overline{u'v'}$contour is the isopleth of $\overline{u'v'} = 0$. Symbols of + and × represent the local peaks over the cylinder and in the near wake region, respectively.

upper shear layer is larger than the magnitude of $\overline{u'v'}$ peak in the lower shear layer, irrespective of the aspect ratio, except in the AR2 case.

In the TKE contours, the level of turbulence kinetic energy rises as the streamwise distance increases from the leading edge and reaches peak values in the near wake region in the AR1, AR2 and AR3 cases. In the AR4 and AR5 cases, on the other hand, distinct peaks are also observed over the cylinders with comparable magnitudes, $0.33U_e^2 \pm 0.01U_e^2$, and at approximately the same location, (x/h = -1.95, y/h = 0.45). The TKE peaks in the wake region show similar values for the AR1 and AR2 cases but decrease as the aspect ratio increases. It is also noted that the TKE and $\overline{u'v'}$ peaks in the near wake region occur at the same streamwise location in the AR1 case, x/h = 3.42. In the AR2 case, however, the TKE peak location, $x/h = 4.10$, is further downstream of the $\overline{u'v'}$ peak locations, $x/h \approx 3.32$.

The peak values of $\overline{u'u'}$ and $\overline{v'v'}$ above the cylinder and in the wake region are shown in Figures 4.6(a-c), respectively. Due to the similar frontal face and separation point at the leading edge of the trapezoidal and rectangular cylinders, there are no evident aspect ratio and body geometry effects in the peak values of $\overline{u'u'}$ above the cylinders (Figure 4.6(a)). The present and previous results for AR $\geq$ 2 are within $\overline{u'u'}/U_e^2 = 0.13U_e^2 \pm 0.03U_e^2$. However, aspect ratio effects are evident in the distributions of the peak values of $\overline{u'u'}$ (Figure 4.6(b)) and $\overline{v'v'}$ (Figure 4.6(c)) in the wake region. As the aspect ratio increases, $\overline{u'u'}$ tends to decrease linearly and approximately fits the function, $\overline{u'u'}/U_e^2$ = -0.041AR + 0.273. Meanwhile, $\overline{v'v'}$ shows a similar peak value of $0.30U_e^2$ at AR $\leq$ 3 and then decreases to $0.08U_e^2$ at AR $\geq$ 4. Compared to the rectangular cases, a significant difference is observed at AR = 1 (Figure 4.6(c)), where the $\overline{v'v'}$ peak in the AR1 rectangular case is more than twice the value for the AR1 trapezoidal case. The comparatively

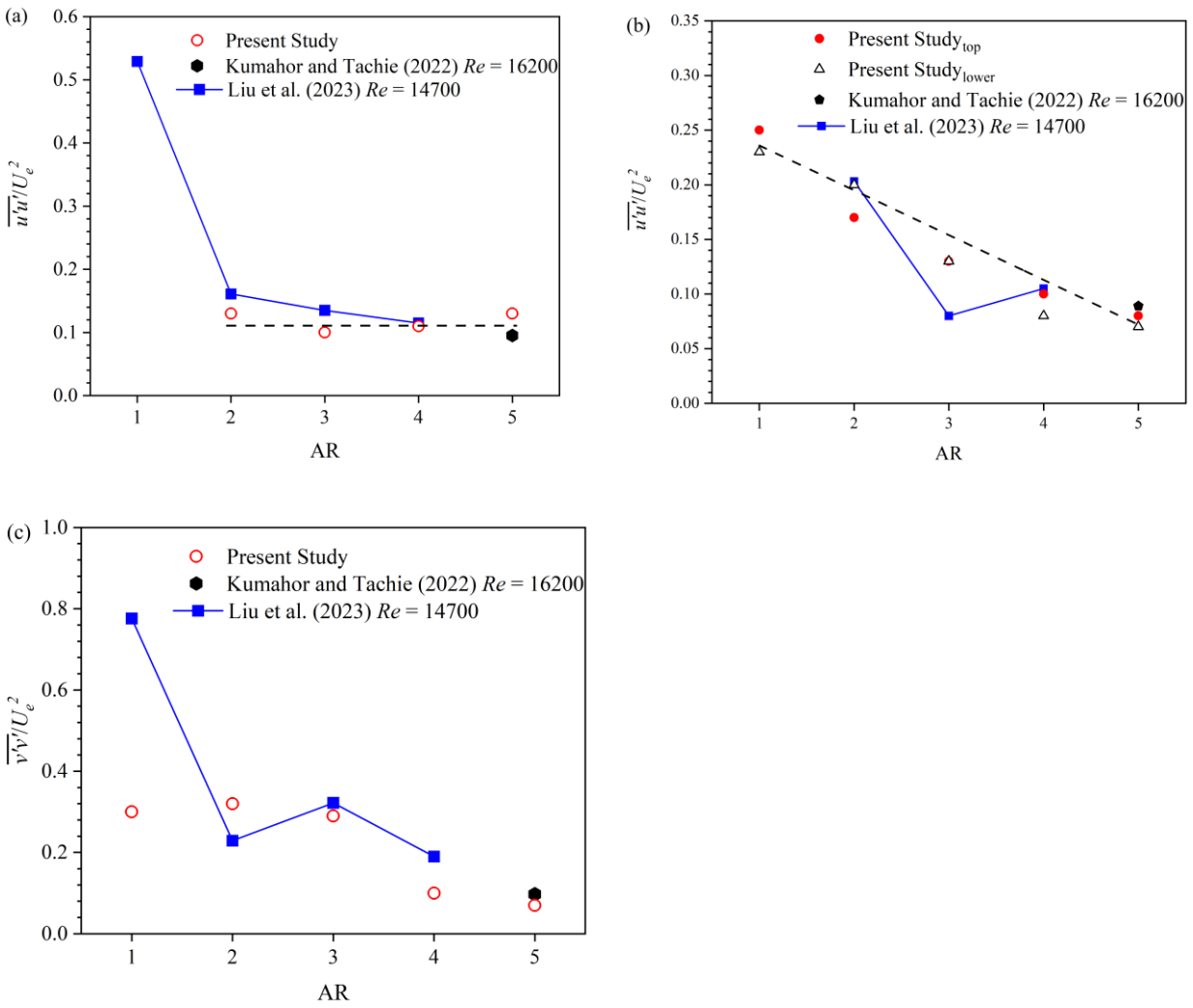

Figure 4.6: Distributions of peak values of streamwise Reynolds normal stress ($\overline{u'u'}$) above the cylinder, (a), and peak values of Reynolds normal stresses ($\overline{u'u'}$ and $\overline{v'v'}$) in the wake region, (b) and (c), respectively.

smaller $\overline{v'v'}$ behind the AR1 trapezoidal case is consistent with the observation by Nakagawa et al. (1999) and Liu et al. (2022b) that a larger recirculation region (shown in Figure 4.1) is always associated with smaller turbulent intensities in the wake region.

4.3 Turbulent Transport and Production of Turbulent Kinetic Energy

The turbulent transport of TKE by the streamwise fluctuating velocity (u') and vertical fluctuating velocity (v') are examined in terms of third order moments, and are shown in Figure 4.7. In particular, $\left(\overline{u'u'u'} + \overline{u'v'v'}\right)$ represents the turbulent transport of instantaneous TKE by u' and $\left(\overline{u'u'v'} + \overline{v'v'v'}\right)$ represents the turbulent transport of instantaneous TKE by v'. Above the cylinder, contours of $\left(\overline{u'u'u'} + \overline{u'v'v'}\right)$ show a positive region above the mean separating streamline and a negative region beneath the mean separating streamline, but the pattern is reversed in $\left(\overline{u'u'v'} + \overline{v'v'v'}\right)$ contours, irrespective of the aspect ratio. It is observed that the high-speed sweep events with $u' > 0$ and $v' < 0$ beneath the mean separating streamline, transport TKE downward and toward the cylinder while low-speed ejection events with $u' < 0$ and $v' > 0$ above the mean separating streamline, transport TKE upward and away from the cylinder. The switching of sweep and ejection events, along the mean separating line, was also observed above rectangular cylinders with different aspect ratios and Reynolds numbers in uniform flow (Kumahor and Tachie, 2022; Liu et al., 2023), wall mounted rectangular cylinders (Fang and Tachie, 2020; Chalmers et al., 2021) and a square cylinder with various gap ratios (Addai et al., 2022). It is also noted that the location of the event switches is away from the body above the upper tailing edge of the AR1, AR2, and AR3 trapezoidal cylinders, but close to the upper surface in the longer cases, due to the flow reattachment occurs only on the AR4 and AR5 cylinders. With the exception of the positive peak in the $\left(\overline{u'u'v'} + \overline{v'v'v'}\right)/U_e^3$ in the AR3 case, the magnitudes of both positive and negative peak values in the wake region decrease as the aspect ratio increases, irrespective of the transport of TKE by u' or v'. Additionally, the positive peaks in $\left(\overline{u'u'u'} + \overline{u'v'v'}\right)/U_e^3$ contour are comparatively smaller than the negative peaks but reversed in $\left(\overline{u'u'v'} + \overline{v'v'v'}\right)/U_e^3$

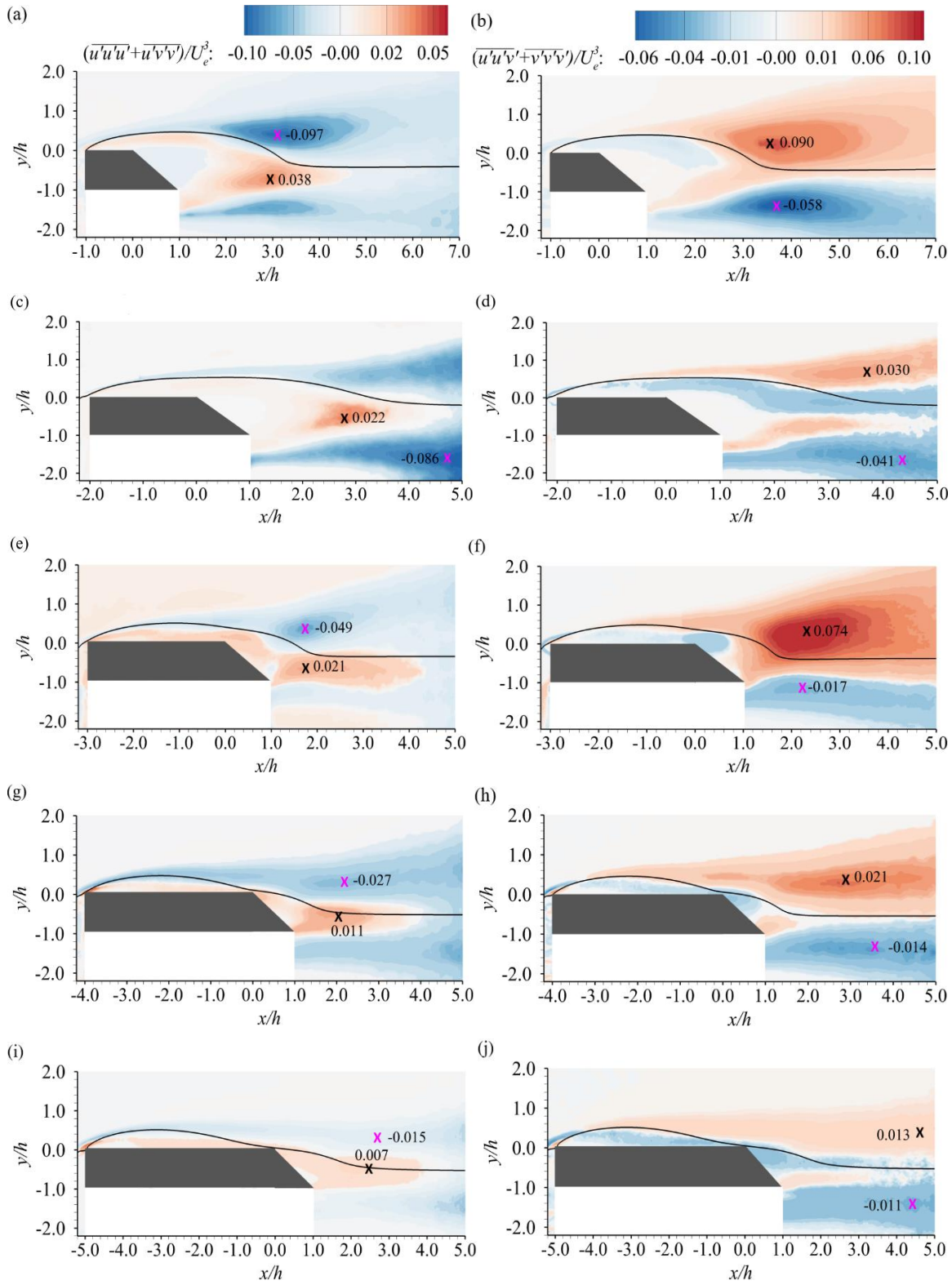

Figure 4.7: Contours of the third order moments $\left(\overline{u'u'u'}+\overline{u'v'v'}\right)/U_e^3$, (a), (c), (e), (g) and (i), and $\left(\overline{u'u'v'}+\overline{v'v'v'}\right)/U_e^3$, (b), (d), (f), (h) and (j) superimposed mean separating streamlines. Symbol × represents the local peaks in the near wake region.

contours, except in the AR2 case. Also, both $\left(\overline{u'u'u'} + \overline{u'v'v'}\right)/U_e^3$ and $\left(\overline{u'u'v'} + \overline{v'v'v'}\right)/U_e^3$ contours show that the furthest peak locations are in the AR2 case, which is consistent with the observation by Liu et al. (2022a) for the rectangular cases.

Figure 4.8 shows contours of the production term of the turbulent kinetic energy for the five tested cases. According to Nematollahi (2019) and Amorin (2020), the production term in the turbulent kinetic energy transport equation of a spanwise homogeneous flow is given by:

$$P_T = -\left(\overline{u'u'}\,\partial U/\,\partial x + \overline{v'v'}\,\partial V/\,\partial y + \overline{u'v'}(\partial U/\,\partial y + \partial V/\,\partial x)\right) \tag{6}$$

The production term was normalized by U_e^3/h. Similar to the Reynolds stresses, the elevated regions of the production term are aligned along the mean separating streamline emanating from the leading edge and are more elongated as the aspect ratio increases. Close to the leading edge of the cylinder, a negative turbulent production region is observed, regardless of the aspect ratios. The same negative production region was also reported by Nematollahi (2019) who investigated the wake flow induced by surface-mounted rectangular cylinders. They illustrated that the negative turbulence production is mainly due to the shear component, $-\overline{u'v'}(\partial U/\,\partial y + \partial V/\,\partial x)$, close to the leading edge of the cylinder. Downstream the leading edge, the transition from negative to positive production occurs within $x < 0.5h$, irrespective of the aspect ratio. A similar transition from positive to negative values also occurs in the contours of Reynolds shear stress in Figure 4.5. As the streamwise distance increases, a positive peak appears above all cylinders with an asymptotic value, $P_T \approx 0.15\, U_e^3/h$, except in the AR3 case, where two positive peaks with the same but smaller magnitude, $P_T = 0.12\, U_e^3/h$, are observed. In the wake region, two positive peaks are observed, irrespective of aspect ratio. Similar to the Reynolds stresses, the magnitudes of the peak are larger in the AR1, AR2 and AR3 cases compared to the AR4 and AR5 cases. It is

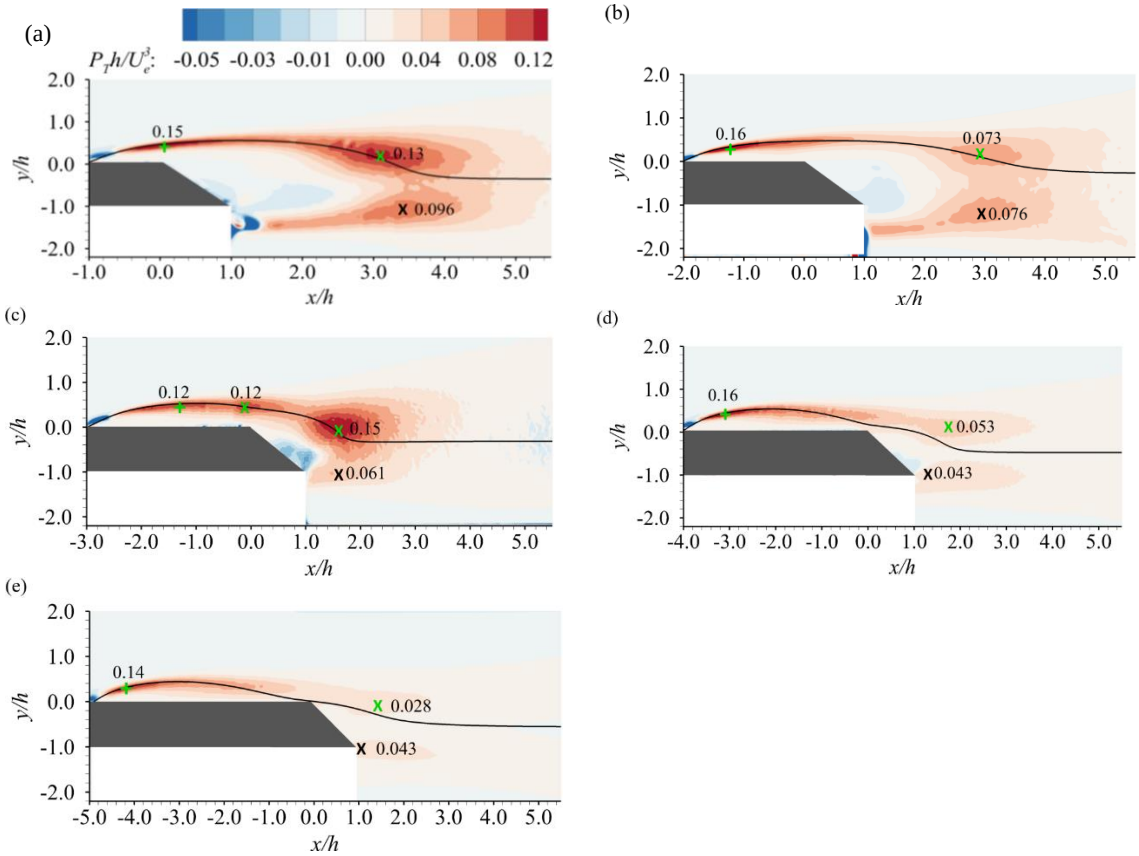

Figure 4.8: Contours of the production term of the turbulent kinetic energy, superimposed mean separating streamlines. Symbols of + and × represent the local peaks over the cylinder and in the near wake region, respectively.

also noticed that the magnitudes and locations of those production peaks are similar to the $\overline{u'v'}$ peaks in the wake region in Figure 4.5, especially in the cases with lower aspect ratios (AR1, AR2 and AR3).

4.4 One-dimensional Profiles of Mean Velocities, Reynolds Stresses and Triple Velocity Correlations.

Figure 4.9 shows distributions of the streamwise mean velocity and Reynolds normal stresses along the centerline in the near wake region. The plots in Figures 4.9(d-f) show the comparison between the trapezoidal cases and rectangular cases with AR = 1, 3 and 5 from

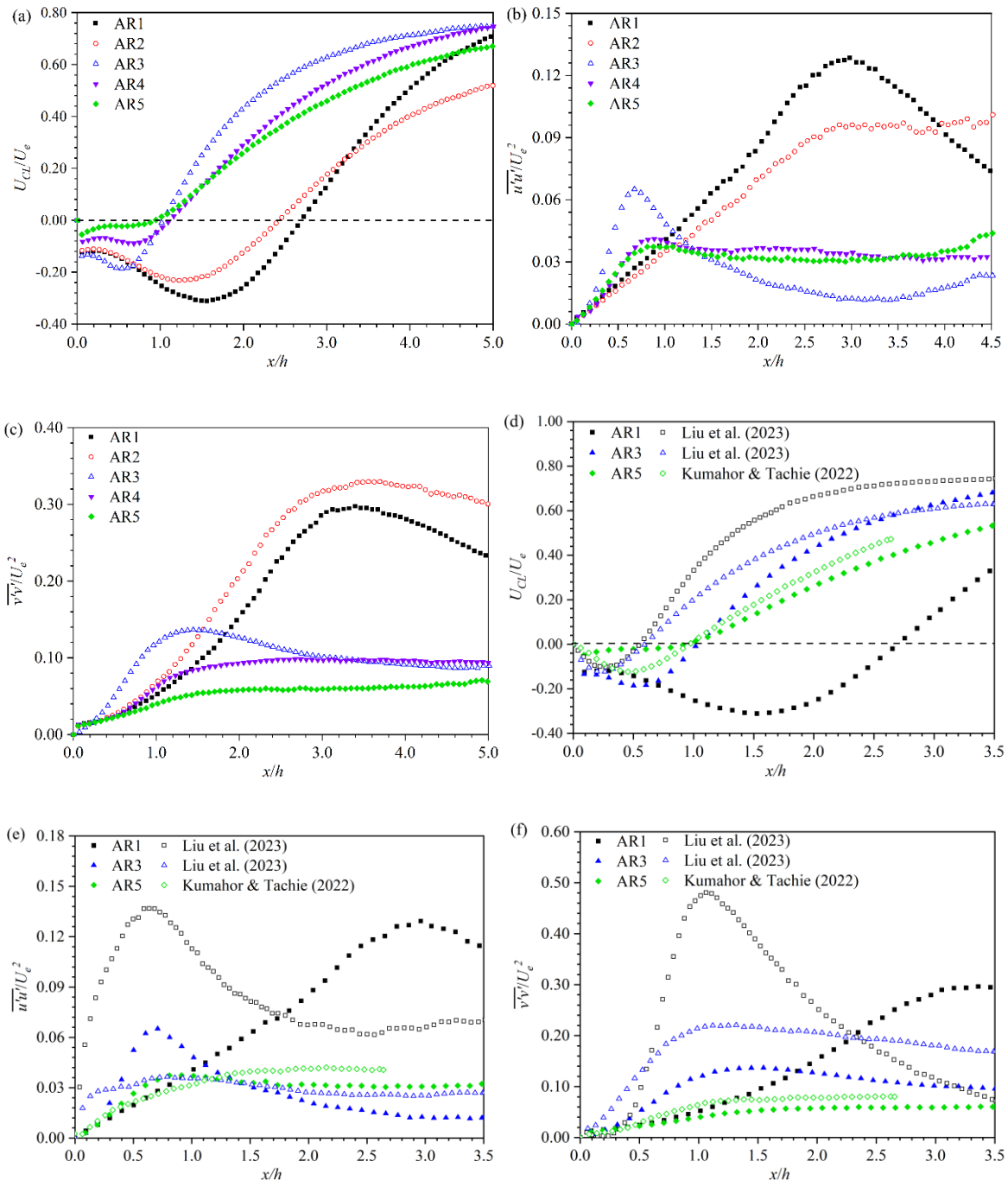

Figure 4.9: Centerline distributions of streamwise mean velocity (U_{CL}), (a), Reynolds normal stresses ($\overline{u'u'}$ and $\overline{v'v'}$), (b) and (c), respectively. Figures (d-f) show the comparison between the present study and rectangular cases of AR1, AR3 and AR5.

Kumahor and Tachie (2022) and Liu et al. (2023). The mean velocity distributions, shown in Figure 4.9(a), are negative within the recirculation region behind the trailing edge and then increase sharply to positive values as the wake flow recovers. The distributions are strongly dependent on the aspect ratio. For example, the streamwise extents of the recirculation region in the AR1 and AR2 cases, defined as the point of intersection of profiles with U_{CL} = 0 (dashed line), are $x/h =$ 2.70 and 2.43, respectively, which are further downstream from the trailing surface of cylinder compared to $x/h = 1.0$ for the larger aspect ratios. The distributions for AR1 and AR2 also recover more slowly compared to the larger aspect ratios. In Figures 4.9(b-c), the Reynolds normal stresses along the centerline of the trapezoidal cylinders increased in the immediate vicinity of the cylinders to maxima and then decrease with increasing streamwise distances as the wake recovered. Meanwhile, the peak values of $\overline{u'u'}$ and $\overline{v'v'}$ for AR3, AR4 and AR5 cases are smaller and closer to the cylinder compared to the cases with smaller aspect ratios.

Figures 4.9(d-f) show that the recirculation region as well as the mean velocity and Reynolds normal stresses along the centerline are also significantly affected by the body geometry, and the differences between the rectangular and trapezoidal cases are more pronounced in the cylinders with smaller aspect ratios (AR1 and AR3) compared to the larger aspect ratio (AR5). For instance, the recirculation regions behind the AR1 and AR3 rectangular cylinders are limited to $x/h = 0.5$, which is shorter than observed for the AR1 and AR3 trapezoidal cases. Furthermore, the AR1 rectangular case shows a more rapid recovery of the mean streamwise velocity compared to the AR1 trapezoidal case. At $x/h = 3.5$, for example, the mean velocity for the AR1 rectangular cylinder has recovered to $0.74U_e$ compared to $0.32U_e$ in the AR1 trapezoidal case. In the case of AR5, however, differences between the trapezoidal and rectangular cylinders are smaller with the former and latter recovering to $0.40U_e$ and $0.46U_e$, respectively, at $x/h = 2.5$. As shown in

Figures 4.9(e) and 4.9(f), differences between the Reynolds stresses along the centerline are also more evident in the AR1 and AR3 cases compared to the AR5 case. For instance, the $\overline{u'u'}$ and $\overline{v'v'}$ distributions of the AR1 rectangular case show higher peak values and the peak locations are closer to the cylinder compared to the AR1 trapezoidal case. In the AR3 cases, the trapezoidal case shows a larger $\overline{u'u'}$ peak but a smaller $\overline{v'v'}$ peak compared to the rectangular case. However, the Reynolds normal stresses for both the rectangular and trapezoidal cases with a larger aspect ratio (AR5) show similar peak values and peak locations (Figures 4.9(e) and 4.9(f)) and tend to collapse as the streamwise distance increases.

Figures 4.10(a-c) show the distributions of recirculation length (L_r) and wake formation lengths ($L_{u'}$ and $L_{v'}$). The recirculation length is measured from the trailing edge of the cylinder to the location where *U* reaches zero along the centerline. Figure 4.10(a) shows that L_r can be significantly affected by the streamwise aspect ratio and body geometry. Due to the merging of the wake vortex and primary vortex in the wake region behind AR1 and AR2 trapezoidal cylinders, a stronger reverse flow was produced and hence, the recirculation length in the present study is longer at AR = 1 and 2, compared to larger aspect ratios (AR = 3, 4 and 5). Compared to the rectangular cases, L_r is longer for the trapezoidal cases, irrespective of the aspect ratios. The longest L_r in the rectangular cases is observed at AR = 2 but at AR = 1 in the present study.

The wake formation lengths, $L_{u'}$ and $L_{v'}$, are measured from the upper trailing edge of the cylinder to the maximum locations of $\overline{u'u'}$ and $\overline{v'v'}$, respectively, and their variations with aspect ratios are presented in Figures 4.10(b-c). Similar to the recirculation length, the wake formation lengths for the trapezoidal cases are also larger for AR = 1 and 2 compared to the larger aspect

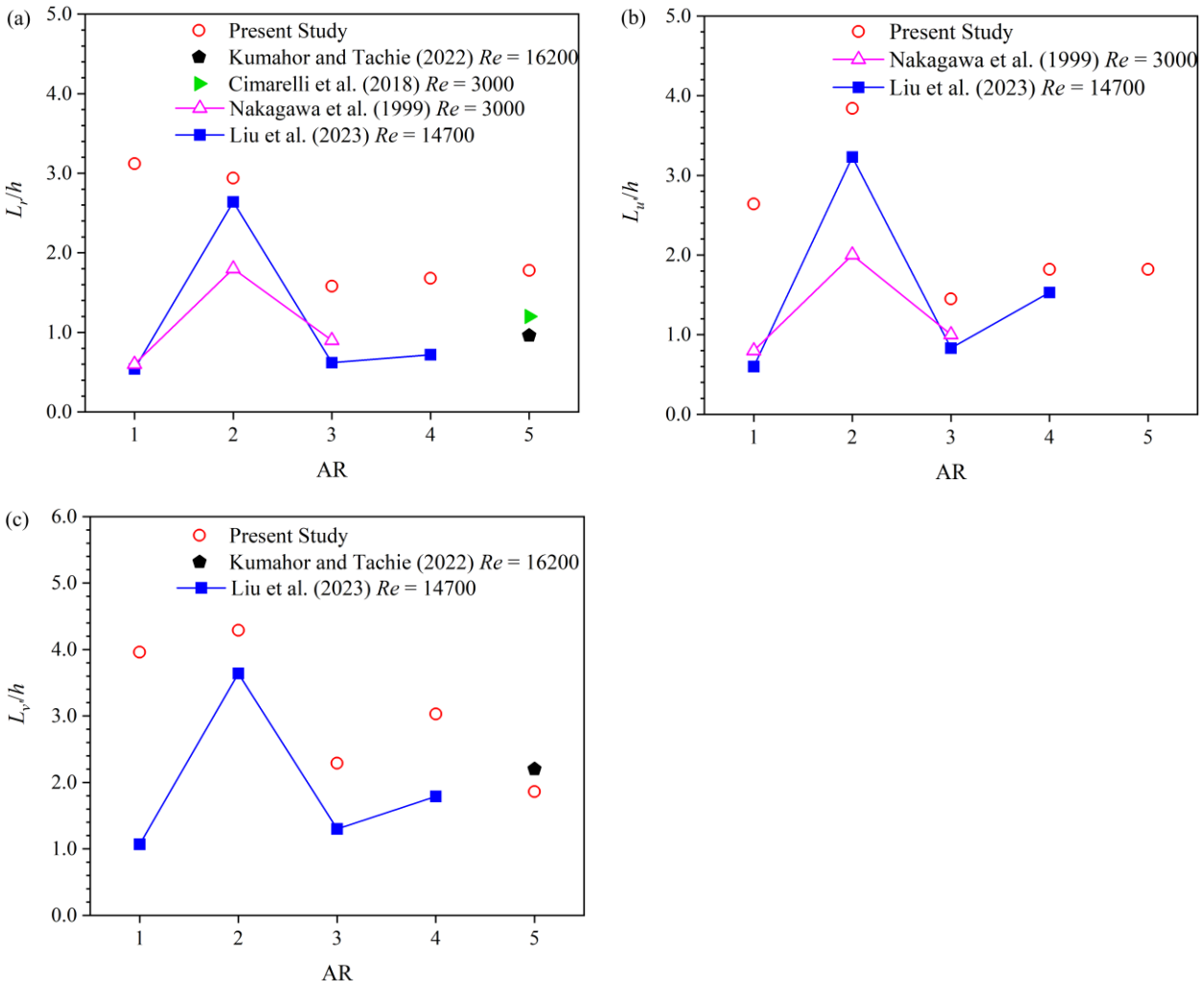

Figure 4.10: One-dimensional distributions of recirculation length (L_r), (a), and the wake formation lengths ($L_{u'}$ and $L_{v'}$), (b) and (c), together with the data of rectangular cases from previous studies.

ratios. Compared to the rectangular cases, both $L_{u'}$ and $L_{v'}$ are consistently larger in the trapezoidal cases, except for AR = 5 in Figure 4.10(c), where no significant difference is observed. Unlike the distribution of L_r, however, both the rectangular and trapezoidal cases show the longest wake formation lengths at AR $= 2$.

To further provide a quantitative comparison among various aspect ratios, one-dimensional vertical profiles of mean velocities and Reynolds stresses at selected streamwise

locations ($x/L =$ -1.0 and -0.5 and $x/h =$ 0.0, 0.5, 1.0, 2.0 and 3.0) are shown in Figures 4.11. Since the front face and separation point are the same, the streamwise mean velocity profiles in Figure 4.11(a) are nearly independent of the aspect ratio at the leading edge ($x/L =$ -1.0). Within the shear layer, a saddle point is developed at $x/L =$ -0.5 due to the formation of the primary vortex. It is also observed that the profiles for the AR1 and AR2 cases at $x/L =$ -0.5 show a faster recovery to uniform flow condition compared to the larger aspect ratios. As the streamwise distance increases from the trailing edge ($x/h = 0.0$), however, the mean profiles of the AR1 and AR2 cases show a slower recovery compared to the larger aspect ratios due to the larger recirculation region and higher magnitudes of reverse flow behind the AR1 and AR2 cylinders, as shown in Figures 4.1(a-b) and 4.3(a). In Figure 4.11(b), the vertical profiles of V show the highest magnitude at the leading edge of the cylinder ($x/L = -1.0$), regardless of the aspect ratio. Due to mean flow reattachment on the AR4 and AR5 cylinders, a sign switch from positive to negative occurs downstream of the leading edge ($x/L = -0.5$) in those cases. On the inclined surface, from $x/h = 0.0$ to $x/h = 1.0$, the V profile of the shorter cylinders (AR1 and AR2) still show positive peaks. This is consistent with the observation in Figure 4.1, where a larger recirculation region is observed behind the AR1 and AR2 cylinders due to the stronger downward flection of the mean flow and slower mean flow recovery in the AR1 and AR2 cases. As the streamwise distance increases, wake double peaks are observed in the wake region, irrespective of the aspect ratio and streamwise location.

The profiles of the Reynolds normal stresses (Figures 4.11 (c-d)) clearly demonstrated that the turbulence field is highly anisotropic. In particular, $\overline{u'u'}$ is significantly higher than $\overline{v'v'}$ above the cylinder but lower than the $\overline{v'v'}$ in the near wake region. This observation is consistent with those made by Moore et al. (2019a) and Kumahor and Tachie (2023a) for rectangular cylinders.

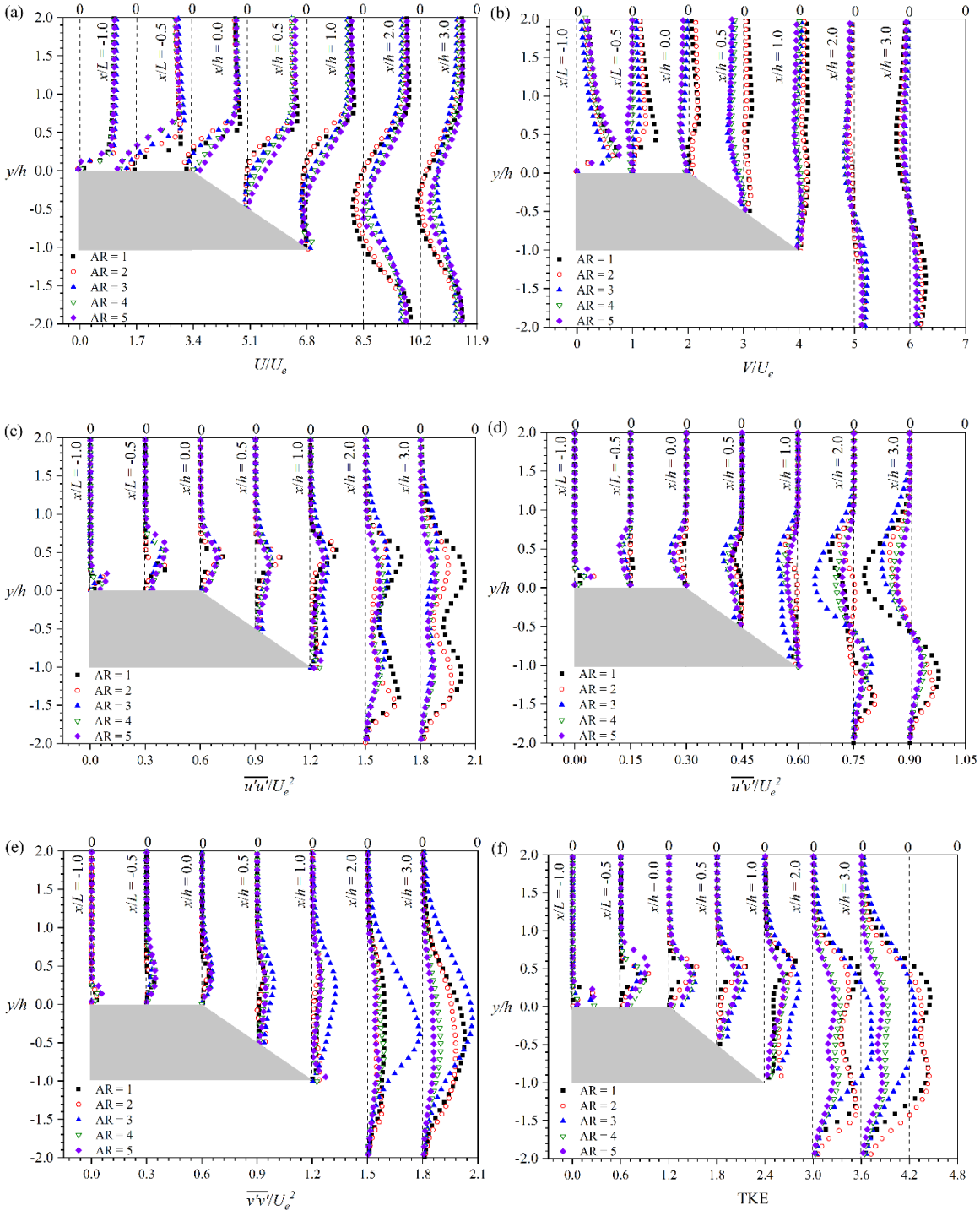

Figure 4.11: One-dimensional vertical profiles of streamwise mean velocity (U), (a), vertical mean velocity (V), (b), Reynolds stresses ($\overline{u'u'}$, $\overline{v'v'}$ and $\overline{u'v'}$), (c), (d) and (e), and TKE, (f), respectively.

As the downstream distance increases, double peaks are observed in the AR3 case at $x/h = 1.0$ (Figure 4.11(c)) but not until $x/h = 2.0$ in other cases. At $x/h = 3.0$, the double peaks are more distinct in the AR1 and AR2 cases compared to the longer cases. In Figure 4.11(c), the peak of the $\overline{v'v'}$ profile of the AR3 case significantly increases, starting from $x/h = 1.0$ until $x/h = 3$, whereas distinct increase in $\overline{v'v'}$ peak for AR1 and AR2 cases is only observed at $x/h = 3.0$. The profiles of Reynolds shear stress ($\overline{u'v'}$) are shown in Figure 4.11(d). Although double peaks are observed in the wake region ($x/h = 2.0$ and 3.0), irrespective of the aspect ratio, the magnitudes of both positive and negative peaks are higher in the AR1, AR2 and AR3 cases compared to the cases with the largest aspect ratios (AR4 and AR5). The profiles of TKE are shown in Figure 4.11(e). The double peaks of TKE are only observed in the AR3 case at $x/h = 1.0$. In the wake region ($x/h = 2.0$ and 3.0), however, the evident double peaks are observed, irrespective of the streamwise aspect ratio.

According to Nematollahi (2019), the structural differences in the Reynolds stress producing motions can be explored by quantitively investigating the triple velocity correlations. Therefore, the vertical profiles of the triple velocity correlations at selected streamwise locations above and behind the cylinders (i.e., x/L = -0.5 and -1.0 and $x/h = 0.0$, 0.5, 1.0, 2.0 and 3.0) for different aspect ratios are presented in Figure 4.12. Although no evident aspect ratio effects are observed above the cylinder, significant differences occur in the wake region. Similar to the vertical profiles of the streamwise Reynolds normal stress, characteristic dual peaks characterize the $\overline{u'u'u'}$ vertical profiles at $x/h = 2.0$ and 3.0 in Figure 4.12(a). Compared to the longer cases (AR3, AR4 and AR5 cases), a more distinct $\overline{u'u'u'}$ double peaks are observed for the shorter cases (AR1 and AR2). Unlike the vertical profiles of Reynolds shear stress, both $\overline{u'u'v'}$ and $\overline{u'v'v'}$

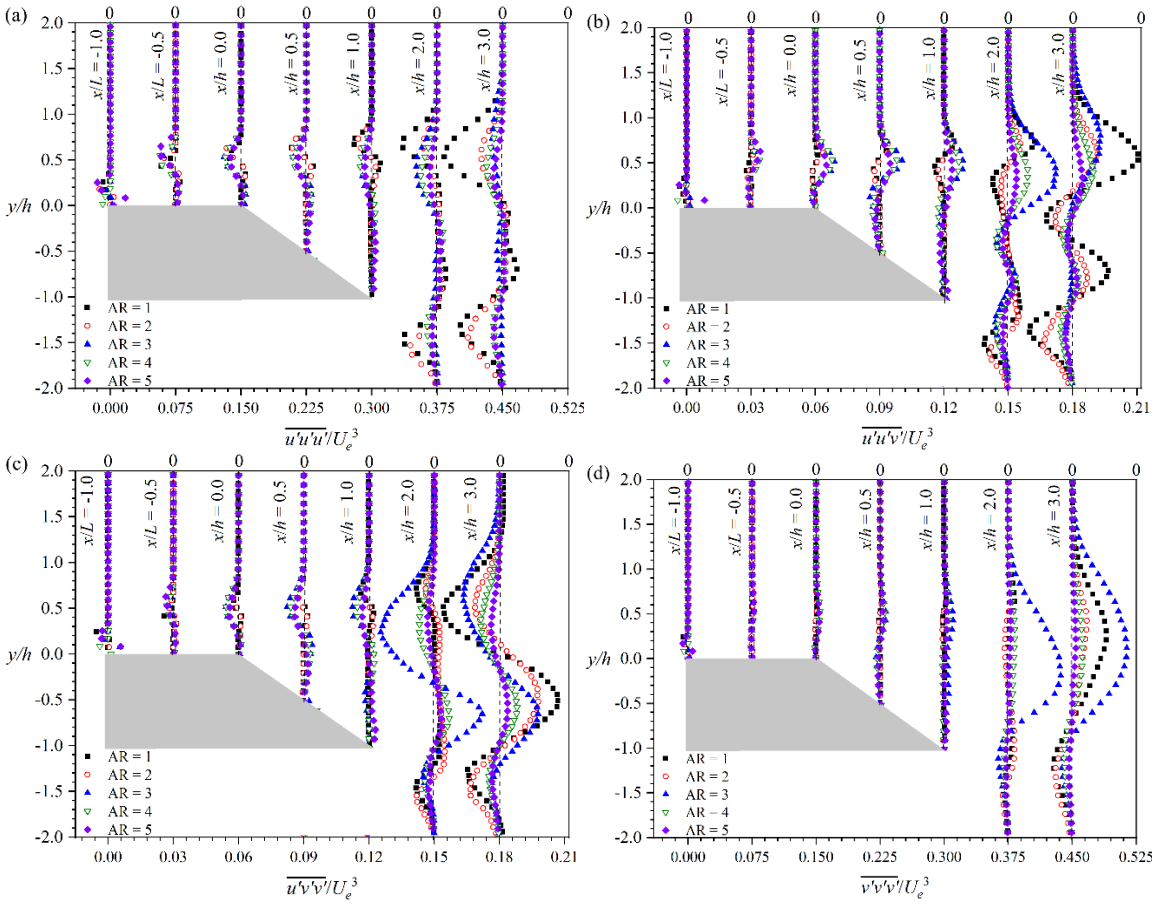

Figure 4.12: One-dimensional vertical profiles of triple velocity correlations, $\overline{u'u'u'}$, $\overline{u'u'v'}$, $\overline{u'v'v'}$ and $\overline{v'v'v'}$, at selected streamwise locations, x/L = -1.0 and -0.5 and x/h = 0.0, 0.5, 1.0, 2.0, and 3.0, respectively.

profiles show multiple peaks in the wake region in Figures 4.12(b-c). The multiple peaks are more evident in the AR3 case at $x/h = 2.0$ in both Figures 4.12(b) and 4.12(c) compared to the other cases. Further away from the cylinder, at $x/h = 3.0$, however, the multiple peaks are more evident in the shorter cases (AR1, AR2 and AR3) in Figure 4.12(b), but are evident, regardless of the aspect ratio in Figure 4.12(c). In Figure 4.12(d), the most notable peak value of $\overline{v'v'v'}$ is observed in the AR3 case at $x/h = 2.0$ and in both AR1 and AR3 cases at $x/h = 3.0$ compared to the other cases.

4.5 Probability Density Function and Joint Probability Density Function

The PDF distributions of the streamwise fluctuating velocity at $\overline{u'u'}_{max}$ location and the vertical fluctuating velocity at $\overline{v'v'}_{max}$ location are presented in Figure 4.13. As shown in Figures 4.13(a-b), the PDF of u' and v' in the present study are strongly dependent on the streamwise aspect ratio. For instance, the distributions of u' in the shorter cases (AR1, AR2 and AR3) in Figure 4.13(a) show an asymmetric bimodal shape and are more negatively skewed in comparison to the unimodal and nearly Gaussian distribution in the AR5 cases. Additionally, positive u', which is indicative of high momentum fluid is more likely than negative u' in the case of the large aspect ratio cylinders. Similar to u', asymmetric bimodal distributions of v' are also observed in the AR1, AR2, and AR3 cases (Figure 4.13(b)). In the cases of AR2 and AR3, however, negative v' associated with vortices shed from the upper trailing edge is more probable than positive v' from the lower shear layer.

Figures 4.13(c-d) show the comparison between the present study and the rectangular cases for AR = 1, 2, and 4 (Liu et al., 2023). In Figure 4.13(c), the AR1 rectangular cylinder shows an asymmetric bimodal u' distribution, but with more distinct peaks compared to the AR1 trapezoidal case, while the AR2 and AR4 rectangular cylinders show a distribution that is approximately Gaussian. In Figure 4.13(d), the distributions of v' for the rectangular cases are bimodal in the AR1 and AR4 cases and unimodal shape in the AR2 case and approximately symmetric about the $v'/v_{rms} = 0$ (Figure 4.13(d)), irrespective of aspect ratio. In the present study, however, an asymmetric unimodal shape is observed in the AR4 case. The symmetric v' distributions for the rectangular cylinders indicate the periodically shed vortices with equal strengths induced by the symmetric upper and lower surfaces of the rectangular cylinder move across the centerline of the

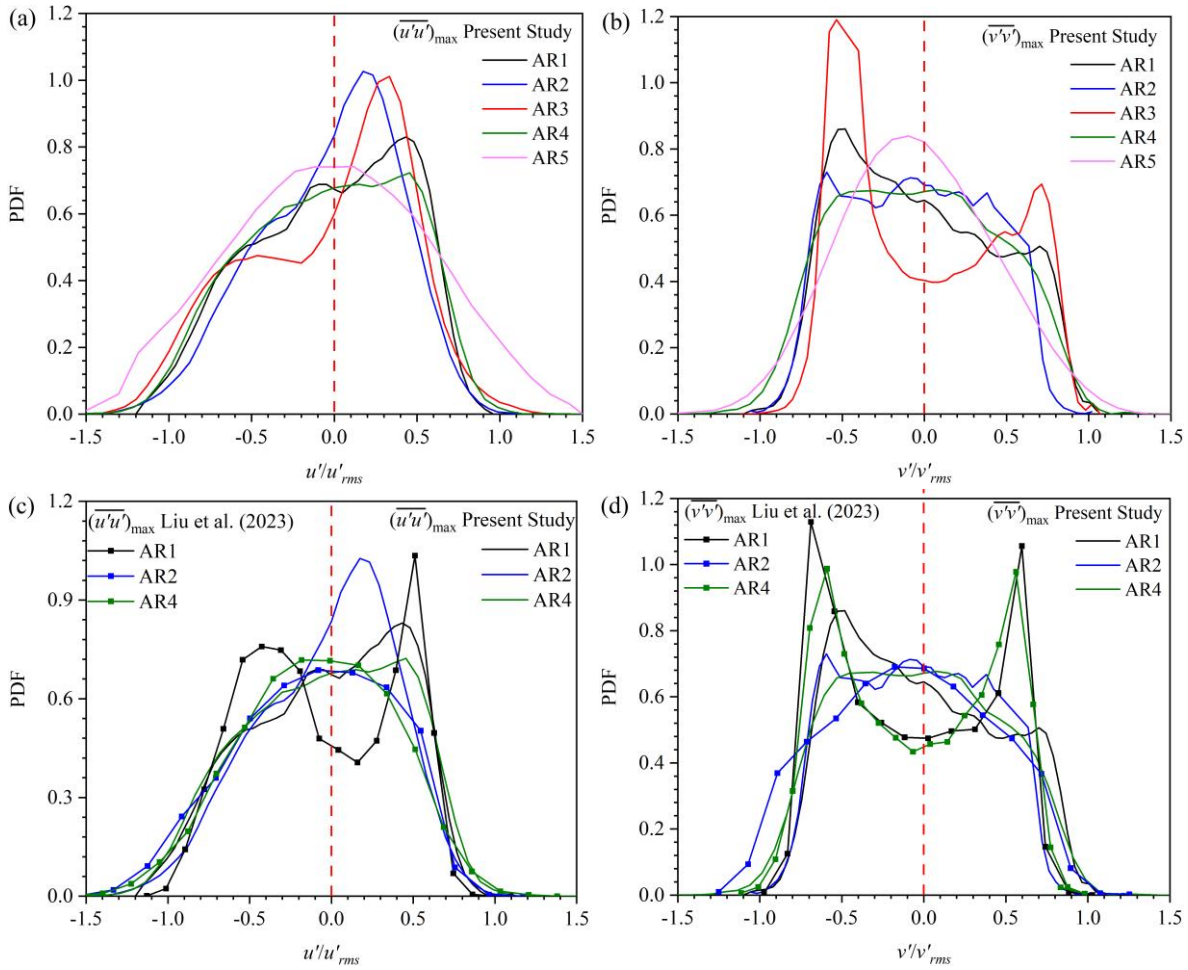

Figure 4.13: Probability density function (PDF) distributions of streamwise fluctuating velocity (u') at the location of $\overline{u'u'}_{max}$, (a), and vertical fluctuating velocity (v') at the location of $\overline{v'v'}_{max}$, (b), of five test cases. Figures (c) and (d) show the comparison between the present study and the rectangular cases of AR1, AR2 and AR4.

cylinder alternatively (Nakagawa et al., 1999). It is likely that the asymmetric distributions of v' in the present study result from positive and negative vortices with unequal strength and shedding frequency induced by the unequal streamwise lengths of the upper and lower surfaces of the trapezoidal cylinder.

Following Wallace and Brodkey (1977) and George (2013), the joint probability density function (JPDF), defined as:

$$\overline{u'v'} = \iint_{-\infty}^{\infty} u'v'P(u', v')\ du'\ dv' \tag{6}$$

is employed to examine the correlation between the instantaneous velocity fluctuations. Figure 4.14 shows the joint probability density function (JPDF) contours of streamwise fluctuating velocity (u') and vertical fluctuating velocity (v') at the locations of $\overline{u'u'}_{max}$, $\overline{v'v'}_{max}$ and $\overline{u'v'}_{max}$ in the wake region of various aspect ratios. The straight lines passing thought the origin divide the plots into four quadrant regions: Q1, Q2, Q3 and Q4. Specifically, Q1 (u', v') and Q2 (-u', v') denote the ejection events of high-speed and low-speed fluid, respectively. Q3 (-u', -v') and Q4 (u', -v') denote the sweep events of low-speed and high-speed fluid, respectively. The JPDF contours clearly show that aspect ratio effects are more evident in the cases with lower aspect ratios (AR1, AR2 and AR3) compared to the cases with larger aspect ratios (AR4 and AR5). At the upper peak location of $\overline{u'u'}$ (Figures 4.14 (a, f, k, p, u)), for example, the distributions are inclined towards Q2 and Q4, irrespective of the aspect ratios, indicating the larger contributions of ejection and sweep events to the mean Reynolds shear stress at this location. In the AR1, AR2 and AR3 cases, the maximum probability shifts to Q4, but no such observation is found in the AR4 and AR5 cases. In Figures 4.14(d, i, n, s, x), the JPDF distributions at the upper peak location of $\overline{u'v'}$ (negative $\overline{u'v'}$ peak location) are also inclined towards Q2 and Q4, which are the same as the observation reported by Liu et al. (2023) for AR1, AR2, AR3 and AR4 rectangular cases. Figures 4.14 (b, g, l, q, v) show the JPDF contours at the lower peak location of $\overline{u'u'}$. Due to the change in the orientation of the mean shear in the lower shear layer, the distributions are inclined towards Q1 and Q3, irrespective of the aspect ratio, except in the AR3 cases, indicating the predominance of outward and inward interactions in the determination of the Reynolds shear stress. The similar trends are also observed in the JPDF contours at the lower peak location of $\overline{u'v'}$ (positive $\overline{u'v'}$

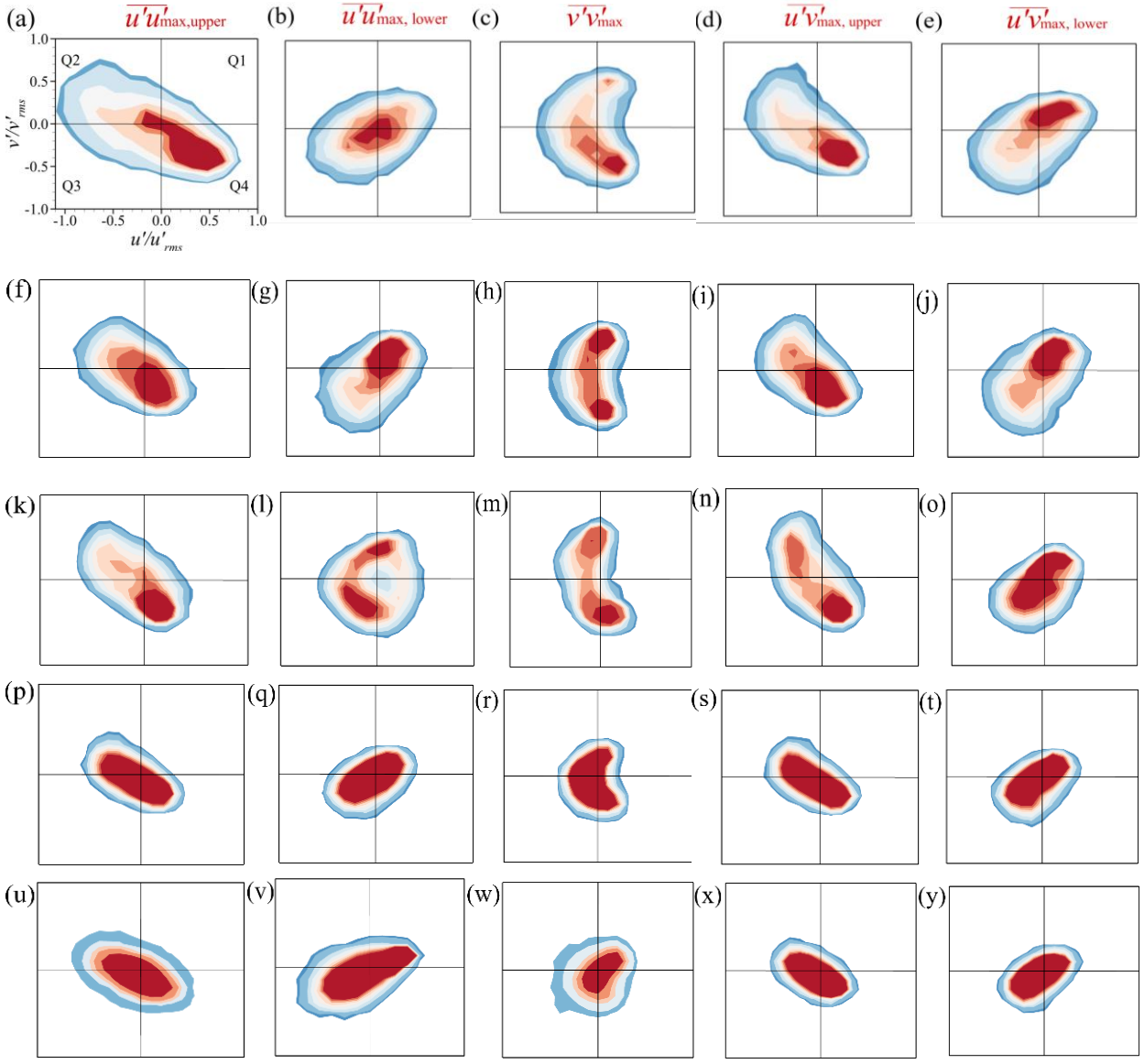

Figure 4.14: Joint probability density function (JPDF) contours of streamwise fluctuating velocity (u') and vertical fluctuating velocity (v') at the locations of $\overline{u'u'}_{max}$, $\overline{v'v'}_{max}$ and $\overline{u'v'}_{max}$, in the wake of five test cases. Contour levels of JPDF at intervals of 0.2 are from 0.0 to 0.8.

peak location), in Figures 4.14(e, j, o, t, y). For the JPDF contours at $\overline{v'v'}_{max}$ (Figures 4.14 (c, h, m, r, w)), the maximum probability in the AR1 and AR3 cases shifts to Q4, however, an approximately symmetric distribution is observed in the AR2 case due to the fact that the location of $\overline{v'v'}_{max}$ is on the symmetry plane and further away from the body compared to the other tested

cases. At the larger aspect ratios, the JPDF contour of the AR5 case trends to toward Q1 and Q3, but no such observation is found in the AR4 case.

4.6 Two-point Autocorrelation and Integral Length Scale

Two-point autocorrelation coefficient, defined in equation (7), is employed to assess the effects of streamwise aspect ratio on the spatial coherency of the large-scale structures above the trailing edge and in the wake region of the trapezoidal cylinders.

$$R_{u_i u_i} = \frac{\overline{u_i'(\boldsymbol{X}_{ref}) u_i'(\boldsymbol{X}_{ref}+\boldsymbol{\Delta X})}}{u_{i,rms}'(\boldsymbol{X}_{ref}) u_{i,rms}'(\boldsymbol{X}_{ref}+\boldsymbol{\Delta X})} \tag{7}$$

where $\boldsymbol{X}_{ref}$ and $\boldsymbol{\Delta X}$ are the reference position and relative displacement, respectively. Figure 4.15 shows the contours of R_{uu} and R_{vv} at the following reference points: ($x/h = 0.0$, $y/h = 0.25$), ($x/h = 1.0$, $y/h =$ -0.5), $\overline{v'v'}_{max}$ and ($x/h = 5.5$, $y/h =$ -0.5). Evidently, the R_{uu} and R_{vv} are sensitive to the streamwise aspect ratios. Above the trailing edge (Figures 4.15(a, c, e, g and i)), for example, R_{uu} extends in both vertical and horizontal directions as the streamwise aspect ratio increases and eventually, show similar shapes at larger aspect ratios (AR3, AR4, and AR5). This implies that the vortices passing the upper trailing edge of the longer cylinders (AR3, AR4, and AR5 cases) tend to maintain their structural integrity compared to the shorter cylinders (AR1 and AR2 cases). The pattern of R_{vv} also expands as the aspect ratio increases (Figures 4.15(b, d, f, h and j)), but a fairly similar shape is only observed over the upper trailing edge of the AR4 and AR5 cylinders. At ($x/h = 1.0$, $y/h =$ -0.5), however, similar shapes are observed in the shorter cases (AR1 and AR2 cases) for both R_{uu} and R_{vv} and are more stretched in the streamwise and vertical directions, respectively, compared to the pattern above the trailing edge. In the AR3 case, both R_{uu}

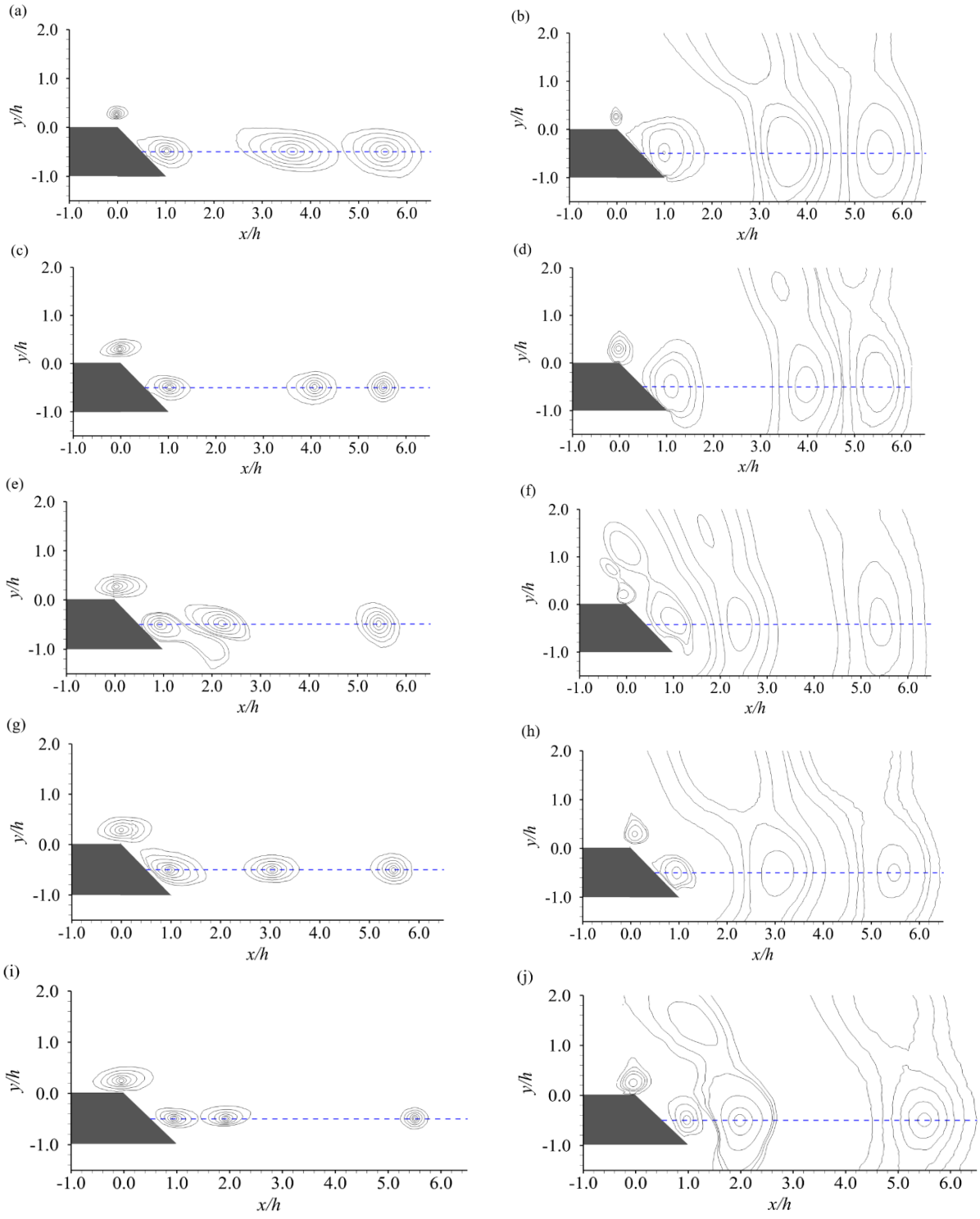

Figure 4.15: Two-point autocorrelations, R_{uu}, (a), (c), (e), (g) and (i), and R_{vv}, (b), (d), (f), (h) and (j), respectively. The selected reference points are at ($x/h = 0.0$, $y/h = 0.25$), ($x/h = 1.0$, $y/h =$ -0.5), $\overline{v'v'}_{max}$ and ($x/h = 5.5$, $y/h =$ -0.5) for five test cases, respectively. Contour levels of R_{uu} at intervals of 0.1 are from 0.4 to 0.9. Contour levels of R_{vv} at intervals of 0.2 are from 0.1 to 0.9.

and R_{vv} show notably different shapes compared to the other cases. As the streamwise aspect ratio increases, the extents of the R_{uu} pattern become smaller in the AR4 and AR5 cases. Further downstream, the R_{uu} patterns of AR1 with reference locations at $\overline{v'v'}_{max}$ and ($x/h = 5.5$, $y/h =$-0.5) are relatively larger in the streamwise direction. However, R_{vv} is less susceptible to changes in aspect ratio and is more stretched in the vertical direction, irrespective of the locations of the reference points.

To quantitatively investigate aspect ratio effects on the spatial coherence of the large-scale structures, the centerline and vertical variations of R_{uu} and R_{vv} with reference locations along the horizontal centerline at x/h = 2.0 and 4.0 are shown in Figure 4.16. Both R_{uu} and R_{vv} distributions clearly show that the large-scale structures in the wake region are highly sensitive to streamwise aspect ratios and the streamwise location of the reference point. In figure 4.16(a), for example, the R_{uu} distributions with different reference locations collapsed reasonably well in the cases with larger aspect ratios (AR4 and AR5), especially in the AR5 case where the R_{uu} is also symmetric about the dashed line of $\Delta x/h$ = 0. In the shorter cases (AR1, AR2 and AR3 cases), the area of the space-correlated region of the autocorrelation (R_{uu} < 0) increases in the AR1 and AR2 cases with the reference location moving further away from the body, except at the positive side of AR2, and decreases in the AR3 case. These results indicate that the inhomogeneous nature of wake flow is more pronounced in the AR1, AR2 and AR3 cases compared to the longer cases. Unlike the R_{uu} centreline distribution, the area of the space-correlated region of the autocorrelation (R_{vv} < 0) in Figure 4.16(b) increases as the streamwise location of the reference point increases, regardless of the aspect ratio. The increased area of the space-correlated region implies the decreased decay rate of the R_{vv} distributions. Figures 4.16 (c-d) show the vertical distributions of R_{uu} and R_{vv}. Due to the limited field of view in the vertical direction, only the

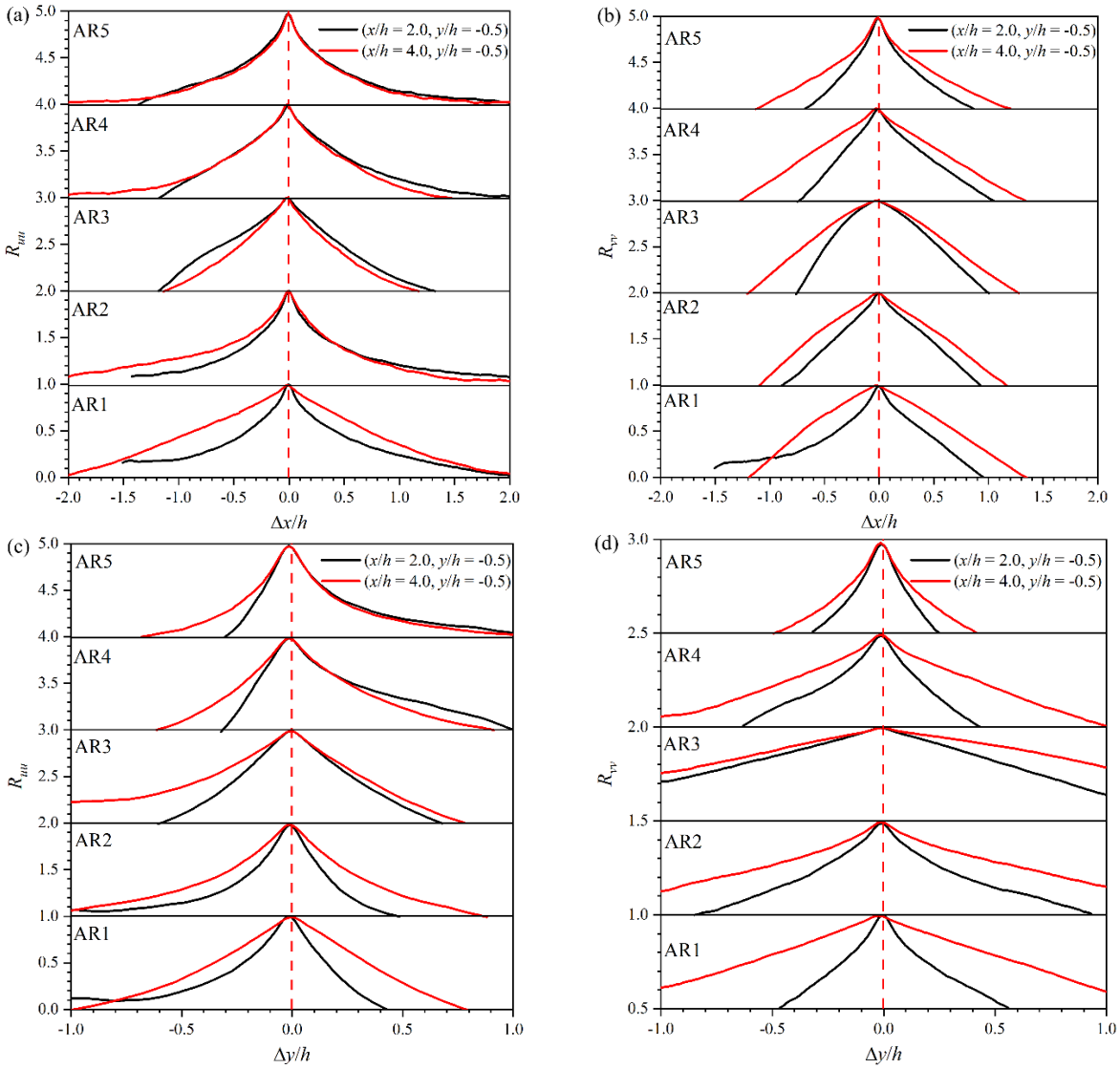

Figure 4.16: Centerline and vertical distributions of R_{uu}, (a) and (c), and R_{vv}, (b) and (d), at reference points, (x/h = 2.0, y/h = -0.5) and (x/h = 4.0, y/h = -0.5), respectively.

distribution of R_{vv} > 0.5 is shown in Figure 4.16(d). Similar to the centreline distributions of R_{vv}, the decay rates of both R_{uu} and R_{vv} vertical distributions decrease as the reference point moves further downstream of the cylinder in the streamwise direction, except the positive side of the largest aspect ratios (AR4 and AR5) in Figure 4.16(c).

The large-scale vortical structures in the wake region are further examined using the integral length scales. According to George (2013), the longitudinal integral length scales based on R_{uu} and R_{vv} are defined as follows:

$$L_{u_i}^{x} = \int_0^s R_{u_i u_i}(\Delta x)\, d(\Delta x) \tag{8}$$

where Δx is the displacement in the streamwise direction with respect to the reference point and s is defined as $R_{u_i u_i}(\Delta x = s) = 0$. Since the flow is inhomogeneous, the integral length scales are evaluated on the positive and negative sides of the reference point, which for R_{uu} are represented by L_u^{-x} and L_u^{+x}, respectively. The corresponding average value of L_u^{-x} and L_u^{+x} is denoted by L_u^a. Similarly, L_v^{-x} and L_v^{+x} are the integral length scales on the positive and negative sides of the reference point for R_{vv} and the corresponding average value is L_v^a. The selected reference locations are along the horizontal centerline of the cylinder, at x/h = 1.0, 1.5, 2.0, 2.5, 3.0, 3.5, 4.0, 4.5, 5.0 and 5.5, respectively. The distributions of the integral length scales shown in Figure 4.17 indicate that the large-scale vortical structures in the wake region are significantly affected by the streamwise aspect ratio and the streamwise locations of the reference point. For example, it is observed that the L_u^{+x} and L_u^{-x} distributions (Figures 4.17(a, c, e, g, i)) tend to collapse in the AR3, AR4 and AR5 cases at the location of $x/h \geq 3.0$, but not for the AR1 and AR2 cases, which further demonstrates the more pronounced inhomogeneity in the near wake region of the AR1 and AR2 cases. Unlike L_u, the L_v^{-x} and L_v^{+x} values shown in Figures 4.17(b, d, f, h, j) collapsed reasonably well farther downstream from the cylinders, x/h > 4.0, irrespective of aspect ratios, except in the AR1 case. For L_v^a, it increases as the reference (with the exception of the AR1 cylinder) and reach asymptotic values of $L_v^a = 0.60h$, $0.68h$, $0.65h$ and $0.43h$ in the AR2, AR3, AR4 and AR5 cases, respectively.

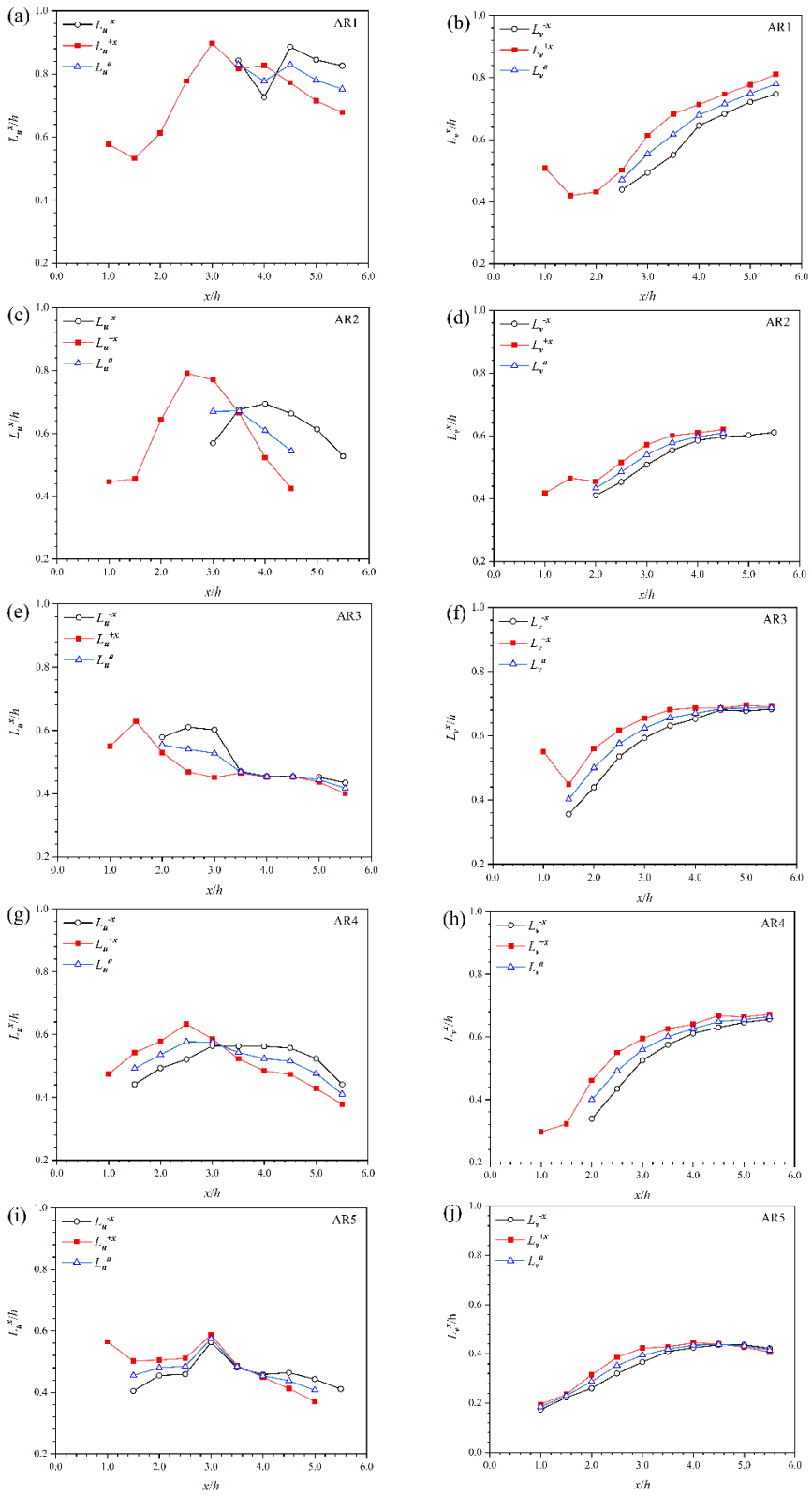

Figure 4.17: Distributions of the integral length scales based on R_{uu}, (L_u^x), and R_{vv}, (L_v^x), respectively. The selected reference points are along the horizontal centerline of the cylinder, at x/h = 1.0, 1.5, 2.0, 2.5, 3.0, 3.5, 4.0, 4.5, 5.0 and 5.5, respectively.

5. CONCLUSION AND RECOMMENDATIONS

The major findings from the present study and recommendations for future work are presented in this chapter.

5.1 Summary and Conclusions

The characteristics of asymmetric wake flows over and behind right-angled trapezoidal cylinders in a uniform flow with streamwise aspect ratios of AR = 1, 2, 3, 4, and 5 are investigated using particle image velocimetry. The mean flow separates at the leading edge and forms a primary vortex over the surface of the longer trapezoidal cylinders (AR3, AR4, and AR5) but extends into the wake region in the AR1 and AR2 cases. A distinct vortex is observed in the lower shear layer of the AR1 and AR2 cylinders but tends to diminish as the aspect ratio increases. Due to the modified trailing edge, part of the recirculating flow in the wake region flows back onto the upper surface of the AR1, AR2 and AR3 trapezoidal cylinders along the inclined surface and hence, mean flow reattachment only occurs on the surface of the AR4 and AR5 cylinders. The vortex cores in the wake region of the AR1 and AR2 cylinders extend further away from the trailing edge in the streamwise direction and the horizontal centerline of the cylinder in the vertical direction compared to the longer cylinders.

The dominant fluctuating velocity component over the cylinder is the streamwise fluctuating velocity, while the vertical fluctuating velocity is dominant in the near wake region due to the alternate vortices shedding from the upper and lower surfaces of the cylinder. Dual peaks of the streamwise Reynolds stress, Reynolds shear stress and production term of the turbulent kinetic energy are observed in the wake region but they are asymmetric about the horizontal centerline.

The turbulent transport of turbulent kinetic energy by streamwise and vertical fluctuating velocities show sign switches along the mean separating streamline, regardless of the aspect ratios. The recirculation length and the wake formation length are longer in the AR1 and AR2 cases compared to the longer cases.

The probability density functions (PDF) of the streamwise fluctuating velocity at the maximum location of streamwise Reynolds normal stress and the vertical fluctuating velocity at the maximum location of the vertical Reynolds normal stress in the near wake region show asymmetric bimodal distributions for the shorter cylinders (AR1, AR2, and AR3) and nearly Gaussian distributions in the longest cylinder (AR5 case). The asymmetry observed in the distributions of the vertical fluctuating velocity is attributed to positive and negative vortices with unequal strength induced by the unequal streamwise lengths of the upper and lower surfaces of the trapezoidal cylinder.

The two-point autocorrelation coefficients of R_{uu} and R_{vv} are sensitive to the streamwise aspect ratios. The distributions of R_{uu} and R_{vv} above the trailing edge expand as the aspect ratio increases and maintain similar shape for the larger aspect ratios (AR4 and AR5). In the wake region, R_{uu} is stretched more in the streamwise location while R_{vv} is more stretched in the vertical direction, irrespective of the aspect ratios.

5.2 Recommendation for the Future work

Based on the findings from the present study, the following recommendations are proposed for future work:

1. The region beneath the cylinder could not be imaged due to the shadow cast by the cylinder. In future studies, it is recommended to investigate the effects of streamwise aspect ratio on the flow beneath the cylinder, as it can differ from the flow above the cylinder due to the asymmetric body geometry of the trapezoidal cylinder.
2. The experiments in the present study were conducted by two-component two-dimension PIV in the $x - y$ plane. As a result, the spanwise velocity component was not measured and the turbulent kinetic energy was estimated based on the two in-plane velocity fluctuations. For future works, it is recommended to use techniques, such as direct numerical simulation, stereoscopic particle image velocimetry or tomographic particle image velocimetry to acquire all three velocity components.
3. According to the literature review in Chapter 2, the Reynolds number can significantly influence the flow dynamics. Therefore, the effects of Reynolds number on the characteristics of the separated shear layer induced by the trapezoidal cylinders are recommended for future works.
4. In future studies, time-resolved PIV and proper orthogonal decomposition (POD) analysis can be applied to the flow fields to reveal the spatial-temporal characteristics of the dominant eddies in the shear layer.

REFERENCES

Achenbach, E., 1968, "Distribution of Local Pressure and Skin Friction around a Circular Cylinder in Cross-Flow up to Re = 5 × 106," Journal of Fluid Mechanics, 34(4), pp. 625–639. DOI: 10.1017/S0022112068002120.

Addai, S., Fang, X., Mante, A. A., and Tachie, M. F., 2022, "The Wake Dynamics Behind a Near-Wall Square Cylinder," Journal of Fluids Engineering, 144(5), 051305. DOI: 10.1115/1.4052675.

Addai, S., Mante, A. A., Kumahor, S., Fang, X. and Tachie, M. F., 2021, "Influence of Wall Proximity on the Wake Dynamics Behind a Square Cylinder," Proceedings of the ASME 2021 Fluids Engineering Division Summer Meeting. Virtual. Online.

Aleyasin, S. S., Tachie, M. F., and Balachandar, R., 2021, "Characteristics of Flow Past Elongated Bluff Bodies with Underbody Gaps due to Varying Inflow Turbulence," Physics of Fluids, 33, 125106, DOI: 10.1063/5.0072390.

Amorin, A. H., 2020, "An Experimental Study of Surface-Mounted Bluff Bodies Immersed in Thick Turbulent Boundary Layers," Master's Thesis, University of Manitoba.

Anagnostopoulos, P., Iliadis, G., and Richardson, S., 1996, "Numerical Study of the Blockage Effects on Viscous Flow Past a Circular Cylinder," International Journal for Numerical Methods in Fluids, 22, no. 11, 1061–74. DOI: 10.1002/(SICI)1097-363(19960615)22:11<1061::AID-FLD393>3.0.CO;2-Q.

Bai, H., and Md, M. A., 2018, "Dependence of Square Cylinder Wake on Reynolds Number," Physics of Fluids, 30, no. 1, 015102. DOI: 10.1063/1.4996945.

Bearman, P. W., and Morel, T., 1983, "Effect of Free Stream Turbulence on the Flow Around Bluff Bodies," Progress in Aerospace Sciences, 20(2-3), pp. 97–123. DOI: 10.1016/0376-0421(83)90002-7.

Bendat, J. S., and Piersol, A. G., 2010, “Random Data: Analysis and Measurement Procedures,” 4th edition, Hoboken, New Jersey: John Wiley and Sons, Inc. DOI: 10.2307/2289430.

Bhattacharyya, S., Izhar, H. K., Shivam, V., Sanjay, K., and Kamal, P., 2022, “Experimental Investigation of Three-dimensional Modes in the Wake of a Rotationally Oscillating Cylinder,” Journal of Fluid Mechanics, 950. DOI: 10.1017/jfm.2022.792.

Bosch, G., and Rodi, W., 1998, “Simulation of Vortex Shedding Past a Square Cylinder with Different Turbulence Models,” International Journal for Numerical Methods in Fluids, 28, pp. 601-616. DOI: 10.1002/(SICI)1097-0363(19980930)28:4<601::AID-FLD732>3.0.CO2-F.

Bruno, L., Salvetti, M. V., and Ricciardelli, F., 2014, “Benchmark on the Aerodynamics of a Rectangular 5:1 Cylinder: An Overview After the First Four Years of Activity,” Journal of Wind Engineering and Industrial Aerodynamics, 126, pp. 87–106. DOI: 10.1016/j.jweia.2014.01.005.

Chalmers, H., Fang, X., Addai, S., and Tachie, M. F., 2022., “The Effects of Wall Roughness on the Flow Dynamics Behind a Near-Wall Square Cylinder,” Experiments in Fluids, 63(8). DOI: 10.1007/s00348-022-03472-z.

Chalmers, H., Fang, X., and Tachie, M. F., 2020, “Streamwise Aspect Ratio Effects on Turbulent Flow Separations Induced by Forward–Backward-Facing Steps,” Journal of Fluids Engineering, 143(2), 021305. DOI: 10.1115/1.4048686.

Chang, X., Chen, W., Huang, Y., and Gao, D., 2022, “Dynamics of the Forced Wake of a Square Cylinder with Embedded Flapping Jets,” Applied Ocean Research, 120. DOI: 10.1016/j.apor.2022.103078.

Chiarini, A., Quadrio, M., and F. Auteri., 2022, “On the Frequency Selection Mechanism of the Low-Re Flow around Rectangular Cylinders,” Journal of Fluid Mechanics, 933. DOI: 10.1017/jfm.2021.1027.

Cimarelli, A., Leonforte, A., and Angeli, D., 2018, “On the Structure of the Self-Sustaining Cycle in Separating and Reattaching Flows,” Journal of Fluid Mechanics, 857, pp. 907–936. DOI: 10.1017/jfm.2018.772.

Dargahi, B., 1989, “The Turbulent Flow Field around a Circular Cylinder,” Experiments in Fluids, 8, no. 1-2, 1–12. DOI: 10.1007/bf00203058.

Dong, S., Karniadakis, G. E., Ekmekci, A., and Rockwell, D., 2006, “A Combined Direct Numerical Simulation–Particle Image Velocimetry Study of the Turbulent near Wake,” Journal of Fluid Mechanics, 569, 185. DOI: 10.1017/s0022112006002606.

Durao, D. F., Heitor, M. V., and Pereira, J. C., 1988, “Measurements of Turbulent and Periodic Flows Around a Square Cross-Section Cylinder,” Experiments in Fluids, 6(5), pp. 298–304. DOI: 10.1007/bf00538820.

Ebenezer, E. E., Tachie, M. F., and Balachandar, R., 2021, “Time-Resolved Wake Dynamics of Finite Wall-Mounted Circular Cylinders Submerged in a Turbulent Boundary Layer,” Journal of Fluid Mechanics, 917, A8. DOI:10.1017/jfm.2021.265.

Ebenezer, E. E., Nematollahi, A., Thacher, E. W., and Tachie, M. F., 2015, “Effects of Upstream Roughness and Reynolds Number on Separated and Reattached Turbulent Flow,” Journal of Turbulence, 16(9), pp. 872–899. DOI: 10.1080/14685248.2015.1033060.

Fang, X., and Tachie, M. F., 2019, “On the Unsteady Characteristics of Turbulent Separations Over a Forward–Backward-Facing Step,” Journal of Fluid Mechanics, 863, pp. 994–1030. DOI: 10.1017/jfm.2018.962.

Fang, X., and Tachie, M. F., 2020, “Spatio-Temporal Dynamics of Flow Separation Induced by a Forward-Facing Step Submerged in a Thick Turbulent Boundary Layer,” Journal of Fluid Mechanics, 267, 353-376. DOI: 10.1017/jfm.2020.209.

Franke, R., Rodi, W., and SchÖnung, B., 1990, “Numerical Calculation of Laminar Vortex-shedding Flow Past Cylinders,” Journal of Wind Engineering and Industrial Aerodynamics, 35, pp. 237-257. DOI: 10.1016/0167-6105(90)90219-3.

George, W. K., 2013, “Lectures in turbulence for the 21st century,” Chalmers University of Technology. Online. Retrieved from: http://www.turbulence-online.com/.

Guissart, A., Andrianne, T., Dimitriadis, G., and Terrapon, V. E., 2019, “Numerical and Experimental Study of the Flow Around a 4:1 Rectangular Cylinder at Moderate Reynolds Number,” Journal of Wind Engineering and Industrial Aerodynamics, 189, pp. 289–303. DOI: 10.1016/j.jweia.2019.03.026.

Heathcote, E., 2017, “How Architects Have Tried to Create ‘Streets in the Sky’,” Subscribe to read Financial Times. Online. Retrieved from: https://www.ft.com/content/8f2bab62-2b32-11e7-bc4b-5528796fe35c.

Herry, B. B., Keirsbulck, L., Labraga, L., and Paquet, J. B., 2011, “Flow Bistability Downstream of Three-Dimensional Double Backward Facing Steps at Zero-Degree Sideslip,” Journal of Fluids Engineering, 133, no. 5. DOI: 10.1115/1.4004037.

Imed, K., Fellouah, H., Ferchichi, M., and Guellouz, M. S., 2014, "Effects of Free-Stream Turbulence and Reynolds Number on the Separated Shear Layer from a Circular Cylinder," Journal of Wind Engineering and Industrial Aerodynamics, 135, 46–56. DOI: 10.1016/j.jweia.2014.10.005.

Kang, J., Kumahor, S., Sagharichi, A., and Tachie, M. F., 2022a, "The Effects of Aspect Ratio on Turbulence Wake Flow Over Right Trapezoidal Prism," Proceedings of ASME Fluids Engineering Division Summer Meeting, Ontario, Canada. DOI: 10.1115/fedsm2022-87640.

Kang, J., Kumahor, S., Sagharichi, A., and Tachie, M. F., 2022b, "Turbulent Characteristics of the Wake Flow Around Rectangular and Trapezoidal Prisms in Uniform Flow," Proceedings of ASME Fluids Engineering Division Summer Meeting, Ontario, Canada. DOI: 10.1115/fedsm2022-87650.

Kang, J., and Tachie, M. F., 2023, "Experimental Study of Turbulent Wake Flow Around Trapezoidal cylinder with Varying Streamwise Aspect Ratios," Journal of Fluids Engineering, 1–49. DOI: 10.1115/1.4062086.

Kang, N., 2021, "Effect of Approach Flow Condition on the Wake of an Ahmed Body," Master's Thesis, University of Windsor.

Khabbouchi, I., Fellouah, H., Ferchichi, M., and Guellouz, M. S., 2014, "Effects of Free-stream Turbulence and Reynolds Number on the Separated Shear Layer from a Circular Cylinder," Journal of Wind Engineering and Industrial Aerodynamics, 135, pp. 46-56. DOI: 10.1016/j.jweia.2014.10.005.

Kiya, M., and Sasaki, K., 1983, "Structure of a Turbulent Separation Bubble," Journal of Fluid Mechanics, 137, pp. 83–113. DOI: 10.1017/s002211208300230x.

Kiya, M., and Tamura, H., 1989, “Flow about a Circular Cylinder in and Near a Turbulent Plane Mixing Layer,” Journal of Fluids Engineering, 111, pp. 124-129. DOI: 10.1115/1.3243612.

Kumahor, S., Addai, S., and Tachie, M. F., 2021, “Interactions between the Shear Layer Emanating from Rectangular Cylinders and the Near Wake Region,” Proceedings of ASME Fluids Engineering Division Summer Meeting, Virtual, online. DOI: 10.1115/fedsm2021-65448.

Kumahor, S., Fang, X., Ediger W. and Tachie, M. F., 2020, “Interactions between the Shear Layer Emanating from Rectangular Cylinders and the Near Wake Region,” Proceedings of the ASME 2021 Fluids Engineering Division Summer Meeting. Virtual, online. DOI: 10.1115/FEDSM2021-65448.

Kumahor, S., Fang, X., and Tachie, M. F., 2022, “Spatio-Temporal Characteristics of Turbulent Flow Separation Around Rectangular and Trapezoidal Prisms in Uniform Flow,” 12th International Symposium on Turbulence and Shear Flow Phenomena, Osaka, Japan. Online. Retrieved from: http://www.tsfp-conference.org/proceedings/2022/249.pdf.

Kumahor, S., Fang, X., Nematollahi, A., and Tachie, M. F., 2021, “The Effects of Upstream Wall Roughness on the Spatio-Temporal Characteristics of Flow Separations Induced by a Forward-Facing Step,” 143(7), 071301. DOI: 10.1115/1.0001627v.

Kumahor, S., and Tachie, M. F., 2022., “Turbulent Flow Around Rectangular Cylinders with Different Streamwise Aspect Ratios,” Journal of Fluids Engineering, 144(5), 051304. DOI: 10.1115/1.4052633.

Kumahor, S., and Tachie, M. F., 2023a, “Turbulent Flow Around a Short Rectangular Cylinder in Uniform Flow at Moderate Reynolds Numbers,” Experimental Thermal and Fluid Science., (under review).

Kumahor, S., and Tachie, M. F., 2023b, “Effects of Streamwise Aspect Ratio on Spatio-temporal Characteristics of Flow around Rectangular Cylinders,” International Journal of Heat and Fluid Flow, 101, 109133. DOI: 10.1016/j.ijheatfluidflow.2023.109133.

Kuroda, M., Tamura, T., and Suzuki, M., 2007, “Applicability of LES to the Turbulent Wake of a Rectangular Cylinder - Comparison with PIV Data,” Journal of Wind Engineering and Industrial Aerodynamics, 95, no. 9-11, 1242–58. DOI: 10.1016/j.jweia.2007.02.004.

Liu, M., Kumahor, S., and Tachie, M. F., 2022a, “Effects of Reynolds Number and Streamwise Aspect Ratio on Turbulent Wakes Generated by Rectangular Cylinders,” Proceedings of ASME Fluids Engineering Division Summer Meeting, Ontario, Canada. DOI: 10.1115/fedsm2022-86964.

Liu, M., Kumahor, S., Audette, L., and Tachie, M. F., 2022b, “Investigations of Aspect Ratio Effects on Wake Dynamics of Rectangular Cylinders,” Proceedings of ASME Fluids Engineering Division Summer Meeting, Ontario, Canada. DOI: 10.1115/fedsm2022-87654.

Liu, M., Kumahor, S., and Tachie, M. F., 2023, “Reynolds Number Effects on Turbulent Wakes Generated by Rectangular Cylinders with Streamwise Aspect Ratio Between 1 to 4,” submitted to Journal of Fluids Engineering.

Lyn, D. A., Einav, S., Rodi, W., and Park, J.-H., 1995, “A Laser-Doppler Velocimetry Study of Ensemble-Averaged Characteristics of the Turbulent Near Wake of a Square Cylinder,” Journal of Fluid Mechanics, 304, pp. 285–319. DOI: 10.1017/s0022112095004435.

Ma, J., Duan, Y., Zhao, M., Lv, W., Wang, J., Meng Ke, Q., and Ren, Y., 2019, “Effect of Airfoil Concavity on Wind Turbine Blade Performances,” Shock and Vibration, 2019, pp. 1–11. DOI: 10.1155/2019/6405153.

Mashhadi, A., Sohankar, A., and Md. M. A., 2021, “Flow over Rectangular Cylinder: Effects of Cylinder Aspect Ratio and Reynolds Number,” International Journal of Mechanical Sciences, 195, 106264. DOI: 10.1016/j.ijmecsci.2020.106264.

Minguez, M., Brun, C., Pasquetti, R., and Serre, E., 2011, “Experimental and High-order LES Analysis of the Flow in Near-wall Region of a Square Cylinder,” International Journal of Heat and Fluid Flow, 32, pp. 558-566. DOI: 10.1016/j.ijheatfluidflow.2011.03.009.

Mohebi, M., Plessix, D. P., Martinuzzi, J. R., and Wood, H. D., 2017, “Effect of Thickness-to-Chord Ratio on the Wake of Two-Dimensional Rectangular Cylinders,” Physical Review Fluids, 2, no. 6. DOI: 10.1103/physrevfluids.2.064702.

Moore, D. M., Letchford, C. W., and Amitay, M., 2019a, “Energetic Scales in a Bluff Body Shear Layer,” Journal of Fluid Mechanics, 875, pp. 543–575. DOI: 10.1017/jfm.2019.480.

Moore, D. M., Letchford, C. W., and Amitay, M., 2019b, “Transitional Shear Layers on Rectangular Sections,” Lecture Notes in Civil Engineering, pp. 519–533. DOI: 10.1007/978-3-030-12815-9_40.

Nakagawa, S., Nitta, K., and Senda, M., 1999, “An Experimental Study on Unsteady Turbulent Near Wake of a Rectangular Cylinder in Channel Flow,” Experiments in Fluids, 27(3), pp. 284–294. DOI: 10.1007/s003480050353.

Narayan, A. R., Zhang, J., Minelli, G., Basara, B., and Krajnović. S., 2019 “Qualitative Assessment of the Bi-Stable States in the Wake of a Finite-Width Double Backward Facing Step,” Journal of Wind Engineering and Industrial Aerodynamics, 186, 241–49. DOI: 10.1016/j.jweia.2019.01.007.

Nematollahi, A., 2019, “Effects of Upstream Roughness on Turbulent Flow over a Forward-Facing Step,” Doctor of Philosophy’s Thesis, University of Manitoba.

Nemes, A., Zhao, J., Lo Jacono, D., and Sheridan, J., 2012, “The Interaction Between Flow-Induced Vibration Mechanisms of a Square Cylinder with Varying Angles of Attack,” Journal of Fluid Mechanics, 710, pp. 102–130. DOI: 10.1017/jfm.2012.353.

Oboe, D., 2023, “Horizontal Axis Wind Turbine Preliminary Blade Design with Xfoil,” MATLAB Central File Exchange. Online. Retrieved from: https://www.mathworks.com/matlabcentral/fileexchange/64745-horizontal-axis-wind-turbine-preliminary-blade-design-with-xfoil.

Okajima, A., 1982, “Strouhal Numbers of Rectangular Cylinders,” Journal of Fluid Mechanics, 123, pp. 379–398. DOI: 10.1017/s0022112082003115.

Pachpute, S., 2022, “CFD Modeling of Vehicle Aerodynamics · CFD Flow Engineering,” CFD Flow Engineering. Online. Retrieved from: https://cfdflowengineering.com/cfd-modelling-of-vehicle-aerodynamics/.

Portela, F. A., Papadakis, G., and Vassilicos, J. C., 2017, “The Turbulence Cascade in the Near Wake of a Square Prism,” Journal of Fluid Mechanics, 825, pp. 315-352. DOI: 10.1017/jfm.2017.390.

Schewe, G., 2013, “Reynolds-Number-Effects in Flow around a Rectangular Cylinder with Aspect Ratio 1:5,” Journal of Fluids and Structures, 39, 15–26. DOI: 10.1016/j.jfluidstructs.2013.02.013.

Raffel, M., Willert, C. E., Wereley, S. T., and Kompenhans, J., 2007, “Particle Image Velocimetry,” 3rd edition, Berlin, Heidelberg, Springer-Verlag. DOI: 10.1007/978-3-540-72308-0.

Samimy, M., and Lele, S. K., 1991, “Motion of Particles with Inertia in a Compressible Free Shear Layer,” Physics of Fluids A: Fluid Dynamics, 3(8), pp. 1915–1923. DOI: 10.1063/1.857921.

Schmid, Peter J., and Dan S. Henningson., 2001, “Stability and Transition in Shear Flows,” Applied Mathematical Sciences, 197-252, DOI: 10.1007/978-1-4613-0185-1.

Sciacchitano, A., and Wieneke, B., 2016, “PIV Uncertainty Propagation,” Measurement Science and Technology, 27(8), 084006. DOI: 10.1088/0957-0233/27/8/084006.

Shadaram, A., Fard, M. A., and Rostamy, N., 2008, “Experimental Study of Near Wake Flow Behind a Rectangular Cylinder,” American Journal of Applied Sciences, 5(8), pp. 917–926. DOI: 10.3844/ajassp.2008.917.926.

Shi, L. L., Liu, Y. Z., and Sung, H. J., 2010, “On the Wake with and without Vortex Shedding Suppression behind a Two-dimensional Square Cylinder in Proximity to a Plane Wall,” Journal of Wind Engineering and Industrial Aerodynamics, 98, 492-503. DOI: 10.1016/j.jweia.2010.03.002.

Shimada, K., and Ishihara, T., 2002, “Application of a Modified k-ε Model to the Prediction of Aerodynamic Characteristics of Rectangular Cross-section Cylinders,” Journal of Fluids and Structures, 16(4), pp. 465-485. DOI: 10.1006/jfls.2001.0433.

Sohankar, A., 2006, “Flow over a Bluff Body from Moderate to High Reynolds Numbers Using Large Eddy Simulation,” Computers and Fluids, 35, no. 10, 1154–68. DOI: 10.1016/j.compfluid.2005.05.007.

Spalart, P.R., Jou, W. H., Strelets, M., and Allmaras, S.R., 1997, “Comments on the Feasibility of LES for Wings, and on a Hybrid RANS/LES Approach, in: Advances in DNS/LES,” Presented at the First AFOSR International conference on DNS/LES, Greyden Press;, pp. 137–148. ISBN: 1570743657.

Trias, F. X., Gorobets, A., and Oliva, A., 2015, “Turbulent Flow around a Square Cylinder at Reynolds Number 22,000: A DNS Study,” Computers and Fluids, 123, 87-98. DOI: 10.1016/j.compfluid.2015.09.013.

University of Aberdeen., 2023, “Pipelines and Soil Mechanics - Online Short Course,” On. University of Aberdeen - On-demand Learning. Online. Retrieved from: https://on.abdn.ac.uk/courses/pipelines-and-soil- mechanics/.

Williamson, C. H. K., 1996, “Vortex Dynamics in the Cylinder Wake,” Annual Reviews of Fluid Mechanics, 28, pp. 477-539. DOI: 10.1146/annurev.fl.28.010196.002401.

Wu, C., Ma, S., Kang, C., Lim, T. A., Jaiman, R. K., Weymouth, G., and Tutty, O., 2016, “Vortex-induced Motion of a Square Cylinder at Moderate Reynolds Numbers,” Proceedings of the ASME 2016 35th International Conference on Ocean, Offshore and Arctic Engineering, Busan, South Korea. DOI:10.1115/OMAE2016-54190.

Yao, J., Lou, W., Shen, G., Shen, Y., and Xing, Y., 2019, “Influence of Inflow Turbulence on the Flow Characteristics around a Circular Cylinder,” Applied Sciences, 9, no. 17: 3595. DOI: 10.3390/app9173595.

APPENDIX

A.1 Measurement Uncertainty

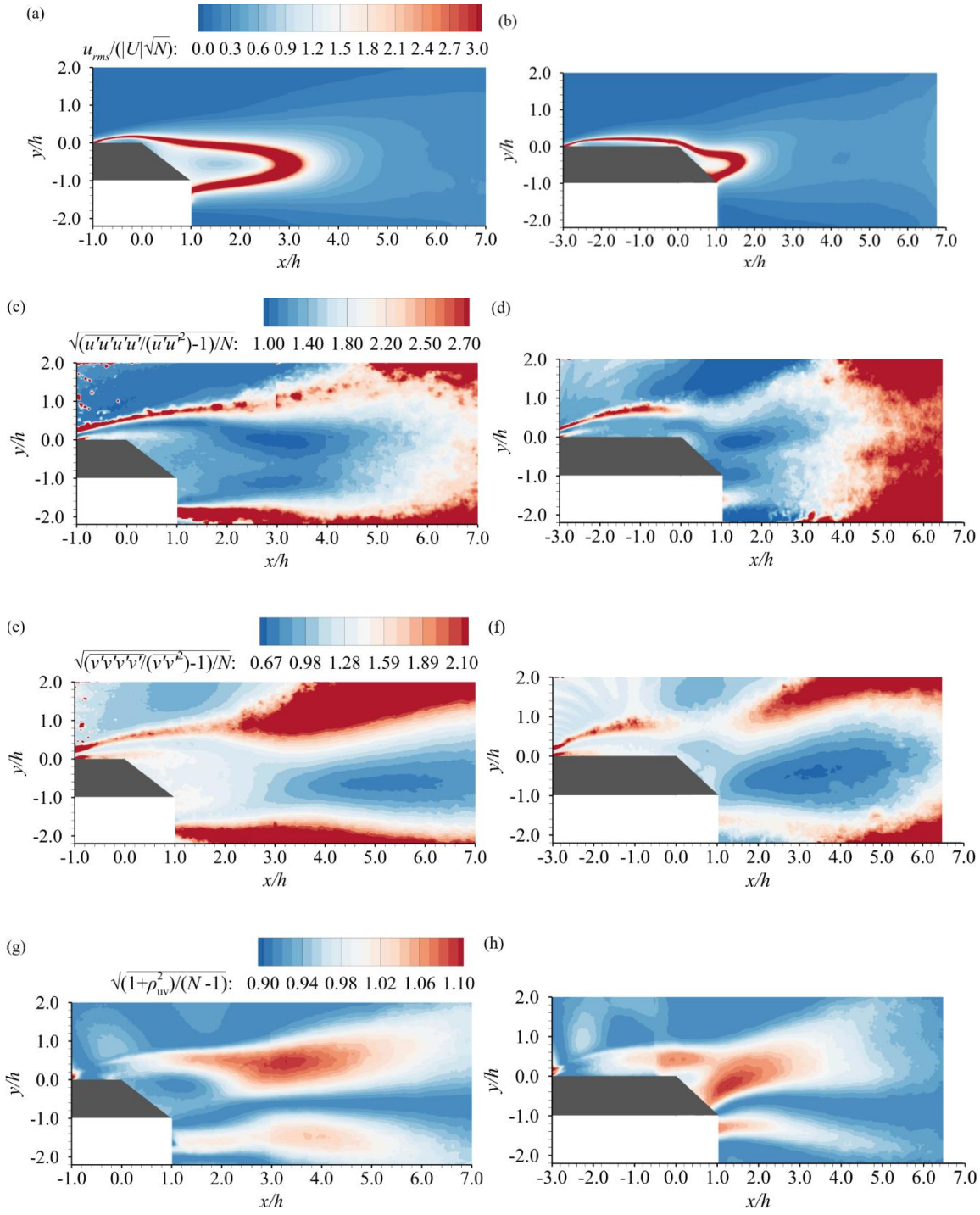

Figure A.1: Contours of uncertainties of streamwise mean velocity, (a-b), and Reynolds stresses, (c-h), for AR1 and AR3 cases, respectively.

A.2 Copyright Form

This is a License Agreement between University of Manitoba ("User") and Copyright Clearance Center, Inc. ("CCC") on behalf of the Rightsholder identified in the order details below. The license consists of the order details, the Marketplace Permissions General Terms and Conditions below, and any Rightsholder Terms and Conditions which are included below.

All payments must be made in full to CCC in accordance with the Marketplace Permissions General Terms and Conditions below.

Order Date	28-Apr-2023	Type of Use	Republish in a thesis/dissertation
Order License ID	1349840-1		
ISSN	0098-2202	Publisher	AMERICAN SOCIETY OF MECHANICAL ENGINEERS,
		Portion	Chapter/article

LICENSED CONTENT

Publication Title	Journal of fluids engineering	Rightsholder	American Society of Mechanical Engineers ASME
Article Title	Experimental Study of Turbulent Wake Flow Around Trapezoidal Cylinders with Varying Streamwise Aspect Ratios	Publication Type	Journal
		Start Page	1
		End Page	49
Author/Editor	AMERICAN SOCIETY OF MECHANICAL ENGINEERS.	Issue	8
		Volume	145
Date	01/01/1973		
Language	English		
Country	United States of America		

REQUEST DETAILS

Portion Type	Chapter/article	Rights Requested	Main product
Page Range(s)	1-15	Distribution	Worldwide
Total Number of Pages	15	Translation	Original language of publication
Format (select all that apply)	Print, Electronic	Copies for the Disabled?	No
Who Will Republish the Content?	Academic institution	Minor Editing Privileges?	Yes
		Incidental Promotional Use?	No
Duration of Use	Life of current edition		
Lifetime Unit Quantity	Up to 499	Currency	CAD

NEW WORK DETAILS

Title	Experimental Study of Turbulent Flow Around Trapezoidal Cylinders in Uniform Flow	Institution Name	University of Manitoba
		Expected Presentation Date	2023-04-24
Instructor Name	Jinhao Kang		

Order Reference Number	N/A	**The Requesting Person/Organization to Appear on the License**	University of Manitoba

REQUESTED CONTENT DETAILS

Title, Description or Numeric Reference of the Portion(s)	Experimental Study of Turbulent Wake Flow Around Trapezoidal Cylinders with Varying Streamwise Aspect Ratios	**Title of the Article/Chapter the Portion Is From**	Experimental Study of Turbulent Wake Flow Around Trapezoidal Cylinders with Varying Streamwise Aspect Ratios
Editor of Portion(s)	Kang, Jinhao; Tachie, Mark F.	**Author of Portion(s)**	Kang, Jinhao; Tachie, Mark F.
Volume of Serial or Monograph	145	**Issue, if Republishing an Article From a Serial**	8
Page or Page Range of Portion	1-49	**Publication Date of Portion**	2023-07-31